Parabolic resonances in 3 degree of freedom near-integrable Hamiltonian systems

Anna Litvak-Hinenzon*, Vered Rom-Kedar

The Faculty of Mathematics and Computer Sciences, The Weizmann Institute of Science, P.O. Box 26, Rehovot 76100, Israel

Abstract

Perturbing an integrable 3 degree of freedom (d.o.f.) Hamiltonian system containing a normally parabolic 2-torus which is m-resonant ($m = 1$ or 2) creates a parabolic m-resonance (m-PR). PRs of different types are either persistent or of low co-dimension, hence they appear robustly in many applications. Energy–momenta bifurcation diagram is constructed as a tool for studying the global structure of 3 d.o.f. near-integrable systems. A link between the diagram shape, PR and the resonance structure is found. The differences between the dynamics appearing in 2 and 3 d.o.f. systems exhibiting PRs are studied analytically and numerically. The numerical study demonstrates that PRs are an unavoidable source of large and fast instabilities in typical 3 d.o.f. systems. © 2002 Elsevier Science B.V. All rights reserved.

PACS: 02.30.Hq; 05.45.+b; 92.60.E; 52.25.F

Keywords: Instabilities; Transport; Chaos

1. Introduction

Two fundamental differences between the phase space structure of 2 and 3 degree of freedom (d.o.f.) near-integrable Hamiltonian systems have attracted much of the scientific interest in recent years. The first difference is that for the 3 d.o.f. case KAM tori do not bound phase space regions as they do in the 2 d.o.f. case and the second difference is that resonance surfaces intersect each other densely on almost all energy surfaces in the 3 d.o.f. case whereas in the 2 d.o.f. case they intersect each other only at the origin, on the zero energy surface (see [1,3,4]). The "Arnold diffusion" (diffusion along resonances, see e.g. [2,5,6,10,12,17,25,30,37,38] and references therein) and *diffusion across resonances* [17] scenarios associated with these resonance webs were the focus of many recent works. Indeed, resonance interactions play a major role in the higher-dimensional apparatus (see e.g. [17] and references therein). Other differences clearly exist: e.g., it is well known that the behavior near fixed points becomes more complex as the dimension of the system is increased. Here, we describe another pan of the complexity of phase space structure which appears in higher-dimensional systems—the appearance of low-dimensional resonant tori with degenerate normal stability—we call such a structure parabolic resonance (PR). In this paper, we discuss

---

* Corresponding author. Present address: Mathematics Institute, University of Warwick, Gibbet Hill Road, Coventry CV4 7AL, UK.
E-mail addresses: litvak@maths.warwick.ac.uk (A. Litvak-Hinenzon), vered@wisdom.weizmann.ac.il (V. Rom-Kedar).

the appearance of PRs in 3 d.o.f. systems and in subsequent paper [27] we discuss the higher-dimensional cases. We devote much of the paper to describe the construction of bifurcation diagrams in the space of constants of motion. This generalizes the shaded energy–momentum diagram developed for the 2 d.o.f. systems in [35]. We propose that such a diagram, which presents global information (in phase space and in energy) regarding the structures of the integrable system is essential for understanding the system behavior under small perturbation.

Systems which exhibit PRs appear in many applications; indeed, in [26,27] we prove that PRs are generic and *persistent* [1] in a class of near-integrable n d.o.f. Hamiltonian systems depending on p parameters provided $n \geq 2$ and $n + p \geq 3$ (notice that for $n \geq 3$, PRs appear persistently even in systems which do not depend on external parameters). For example, PR was discovered while investigating a 2 d.o.f. model describing the motion of weather balloons on geopotential surfaces of the earth atmosphere [32,35,36]. In Section 3, a 3 d.o.f. model extension of this model is discussed. Other examples where PRs appear are the Duffing equation with a k-torus attached to it (the tori represent the effect of neutral modes), and a reduction of the nonlinear Srödinger equation ([18] and references therein) to a six-dimensional Hamiltonian ODE.

Recall the phase space structure of 3 d.o.f. near-integrable Hamiltonians. Typically, in the completely integrable case (with compact level curves) the phase space is foliated by invariant tori on which quasi-periodic/periodic motion occurs. The subject of their persistence in near-integrable Hamiltonian systems has been extensively studied in this century; the KAM theory [3] assures that the majority of the maximal dimensional invariant tori, satisfying some non-degeneracy and Diophantine conditions, persist under small Hamiltonian perturbations (hereafter perturbations will always mean Hamiltonian perturbations). These invariant tori play a major role in 1 and 2 d.o.f. systems. The solutions of such perturbed systems are either confined on KAM tori or trapped between pairs of them, and hence cannot wander arbitrarily far in the phase space. The KAM theory is true for higher-dimensional systems as well, but in 3 or more d.o.f., the co-dimension of the invariant tori on the energy surface is larger than one, hence they do not bound the motion in phase space.

A lower dimensional torus is a torus (here a circle or a 2-torus) with a vector of inner frequencies ω, of dimension smaller than the number of d.o.f. (here, 3), and a vector of multipliers (here, four- or two-dimensional) which determines its stability. If the multipliers are purely imaginary, the normal frequencies vector Ω (a two-dimensional (2D) vector or a scalar) is constructed by taking the imaginary parts of one of each complex-conjugate pair [14]. Such lower dimensional tori persist under small perturbations if ω satisfies certain Diophantine conditions and if, additionally, either the tori are normally hyperbolic [2] [16] or they are normally elliptic [3] and (Ω, ω) are Diophantine [13,33]. A lower dimensional torus is said to be *normally parabolic* if it has at least one zero multiplier (hence, a *vanishing normal frequency*). Maximal dimensional (here 2D) normally parabolic tori (together with a saddle-center bifurcation scenario) survive small Hamiltonian perturbations under Diophantine conditions on their inner frequencies (for normally parabolic circles, additional Diophantine conditions are required on the elliptic part of Ω) [20]. For more details on quasi-periodic tori and their bifurcations, see e.g. [8,9] and references therein. Summarizing, in the typical near-integrable case, normally elliptic, hyperbolic or parabolic lower dimensional tori persist on Cantor sets of action values consisting of the Diophantine frequency vectors. In the integrable case, there is a zero-dimensional dense set of actions on which resonant [4] tori reside (this set contains all the "holes" of the Cantor set(s) which parameterize the KAM tori). In 3 or more d.o.f. integrable Hamiltonian systems, the families of actions corresponding to resonant tori intersect on energy surfaces, creating a resonance web. Under small

---

[1] By persistent we mean physically that the phenomena is robust—small changes in the form of the integrable system (or the family of systems for phenomena of positive co-dimension) will not alter the results. Mathematically, this means that the systems are persistent on a C^1-open set under C^r ($r \geq 1$) perturbations of the class of integrable Hamiltonian systems of the form $H_0(x, y, I; \mu)$.

[2] Hyperbolic lower dimensional invariant torus is a torus such that its multipliers have a non-zero real part.

[3] Elliptic lower dimensional tori are those with non-zero purely imaginary multipliers.

[4] A torus is said to be resonant if its frequencies are rationally dependent.

Hamiltonian perturbations the resonant tori break into resonant zones and orbits may drift along them far from their initial values (this possible scenario, called Arnold diffusion, is still not well understood, see [3] and references therein). In previous works it has been shown that orbits which start in the vicinity of low dimensional resonant tori, exhibit under small perturbations intricate chaotic motion, see e.g. [18,19] and references therein.

PR occurs in 2 d.o.f. systems when the integrable Hamiltonian possesses a parabolic circle of fixed points. Such a circle is persistent in a one parameter family of 2 d.o.f. integrable Hamiltonian systems [34]. Numerical simulations of systems exhibiting a PR, such as the atmospheric model mentioned above, show that perturbed orbits, starting in the vicinity of a parabolic circle of fixed points, exhibit chaotic behavior which combines hyperbolic homoclinic chaos and elliptic resonance type localizations, while the orbit slowly slides through bifurcations. Although these orbits appear to be chaotic, unless additional degeneracy occurs, they stay relatively close to their initial values (though the instability here is stronger than near a hyperbolic resonance or near an elliptic resonance).

Here we study PRs in 3 d.o.f. systems (see also [26,28]). A *parabolic m-resonance* (m-PR) occurs when a small Hamiltonian perturbation is applied to an integrable 3 d.o.f. Hamiltonian system, which possesses a *normally parabolic m-resonant* 2-*torus* (namely, on the 2D torus m independent resonant conditions are satisfied and the normal frequency of the torus vanishes, where for 3 d.o.f. systems $m = 1, 2$). Numerical experiments suggest that slightly perturbed orbits, starting near the parabolic resonant torus of the integrable system, exhibit complicated behavior and instabilities. If in addition to the existence of an m-resonant parabolic torus in the integrable system, the iso-energetic non-degeneracy condition fails so that a whole family of resonant tori exist on the same energy surface, the near-integrable system exhibits a flat parabolic m-resonance (flat m-PR). In such cases, order one instabilities of slightly perturbed orbits are observed in numerical simulations even in the 2 d.o.f. case [34] (note that for 2 d.o.f. systems only $m = 1$ is possible). Flat PRs may be viewed as the higher-dimensional analog to the stochastic web which appears in degenerate 2D area-preserving maps [39].

The large instabilities that were observed for the atmospheric model mentioned above (see Section 3) with realistic parameters values, correspond mathematically to a *nearly* flat PR, and result in a relatively fast traveling of the weather balloons from the equator to the poles, see [36]. The *tangential PR* [5] models the near-flat case, and it was proved in [34] that it is a co-dimension two phenomenon for 2 d.o.f. near-integrable Hamiltonians. Furthermore, in [34] it was shown that the PR, and the near-flat PR, appear in some common 2 d.o.f. physical models. In [26,27] it is proved that the existence of tangential PR is persistent in the class of 4 d.o.f. near-integrable Hamiltonians without dependence of the system on external parameters (i.e. a co-dimension *zero* phenomenon), and it is demonstrated that in this case the instabilities exhibited by perturbed orbits are maximal.

The paper is ordered as follows. First, we construct the simplest model of a 3 d.o.f. system attaining a PR (using normal form techniques), and describe the construction of the energy–momenta diagrams which supply *global* information regarding the singular points in phase space, including the appearance of different kinds of PRs. We compare between the 2 and 3 d.o.f. cases, and demonstrate the different dynamical scenarios which are associated with the new mechanisms of PRs which appear in the 3 d.o.f. case. A 3 d.o.f. atmospheric model is constructed and used as a test case application for our results on the phenomenological model.

2. A phenomenological model

The simplest model exhibiting PRs (and near-flat PRs) in near-integrable 3 d.o.f. Hamiltonian systems is constructed using normal form techniques; the conditions for existence of parabolic 1 and 2-resonant 2-tori are formulated for the integrable Hamiltonian, and an expansion near these conditions is made.

---

[5] Tangential PR corresponds to failure of the KAM iso-energetic non-degeneracy condition on an infinitesimal neighborhood of tori of mixed stability types in the unperturbed system. See [26,27] for extensive study of this case.

Consider a general near-integrable 3 d.o.f. Hamiltonian system of the form: $H(r, s, u, v, p, q; \mu)$, where μ is a vector of parameters. The integrable part of this system has three constants of motion in involution ($F_0 = H_0$, F_1, F_2). For most values of F (regular values with compact level curves), action–angle coordinates on the 3-tori they define may be introduced. Singular values of F, defined as values for which dF_i are point-wise linearly dependent, correspond to singular, smaller dimensional surfaces. Consider a region of phase space where only one such singular relation occurs. Then, a symplectic non-singular change of variables $(r, s, u, v, p, q; \mu) \rightarrow (x, y, \theta_1, I_1, \theta_2, I_2; \mu)$ may be performed, to two action–angle coordinates I_1, I_2 and θ_1, θ_2 and an additional conjugate pair (x, y), for which the singularity occurs ($\nabla_{(x,y)} H_0 = 0$). The integrable part of the new Hamiltonian is independent of the angles (θ_1 and θ_2) [4] and we denote it by $H_0(x, y, I_1, I_2; \mu)$:

$$H(x, y, \theta, I; \mu, \varepsilon) = H_0(x, y, I; \mu) + \varepsilon H_1(x, y, \theta, I; \mu, \varepsilon). \tag{1}$$

Geometrically, the six-dimensional phase space of a Hamiltonian in the form (1) may be described in the following way. A 2-torus with actions I_1, I_2 and angles θ_1, θ_2) is attached to each point of the (x, y) plane. If the point in the (x, y) plane is an equilibrium, the torus attached to it is an invariant torus with the same normal stability type as of this fixed point. The (x, y) plane is called *the normal plane*, since it determines the normal stability type of the 2-tori attached to it [33]. The motion on the 2-tori is either quasi-periodic (non-resonant) or periodic (resonant).

The conditions for an *integrable* 3 d.o.f. Hamiltonian system with a Hamiltonian in the normal coordinates form $H_0 = H_0(x, y, I_1, I_2; \mu)$, and with the symplectic structure

$$dx \wedge dy + \sum_{i=1}^{2} d\theta_i \wedge dI_i, \quad x, y, I_i \in \mathbb{R}, \ \theta_i \in \mathbb{T}$$

to possesses a normally parabolic resonant 2-torus at the origin, are:

(c1) The fixed point conditions—existence of a fixed point in the (x, y) normal plane:

$$\nabla_{(x,y)} H_0(0, 0, I_1, I_2) = (0, 0). \tag{2}$$

(c2) The parabolicity condition:

$$\det\left(\left. \frac{\partial^2 H_0(x, y, I_1, I_2)}{(\partial x, \partial y)} \right|_{(0,0,0,I_2)} \right) = 0. \tag{3}$$

(c3) The condition on the inner frequencies of the invariant parabolic 2-torus for a 1-resonance, $\langle k, \omega \rangle = 0$, corresponding to some pair $(n, m) \in \mathbb{Z}^2 \setminus \{0\}$, is

$$n\dot{\theta}_1 + m\dot{\theta}_2 = n \left. \frac{\partial H_0}{\partial I_1} \right|_{(0,0,0,0)} + m \left. \frac{\partial H_0}{\partial I_2} \right|_{(0,0,0,0)} = 0. \tag{4}$$

Since a 2-torus may fulfill at most two independent resonance conditions (a 2-resonance), the two independent pairs of integers in condition (4) may be chosen WNLG [6] to be $(1, 0)$ or $(0, 1)$ in the 1-resonance case, and $\{(1, 0), (0, 1)\}$ in the 2-resonance case.

Using a Taylor expansion near conditions c1–c3, several symplectic changes of variables, rescaling, and under some general assumptions which further simplify the model (see Appendix A for details), the simplest near-integrable Hamiltonian (in the normal coordinates setting) attaining a PR is of the form:

$$H_0(x, y, I; \mu) = \tfrac{1}{2}y^2 - I_1(\tfrac{1}{2}x^2) + \eta(\tfrac{1}{3}x^3) + \tfrac{1}{4}x^4 + \alpha_2 I_2 + (\tfrac{1}{2} + \alpha_1)\tfrac{1}{2}I_1^2 + \tfrac{1}{2}I_2^2 + \alpha_3 I_1 I_2, \tag{5}$$

---

[6] If some two general independent vectors of integers are chosen, the two corresponding resonance conditions may be always replaced by the conditions for vanishing of one of the frequencies, (A.1) and (A.2) (see Appendix A), by a symplectic change of coordinates.

$$H_1(x, y, \theta, I; \mu, \varepsilon) = \sum_{i=1}^{2} \varepsilon_i f_i(x, y, I_1, I_2, k_i \theta_i), \tag{6}$$

$$H(x, y, \theta, I; \mu, \varepsilon) = H_0(x, y, I; \mu) + H_1(x, y, \theta, I; \mu, \varepsilon), \tag{7}$$

where f_i $(i = 1, 2)$ are polynomials in x, y, I_1 and I_2, and are 2π periodic in their last argument. The vector of parameters is $\mu = (\alpha_1, \alpha_2, \alpha_3, \eta, k_1, k_2)$ with $\alpha_1, \alpha_2 \in \mathbb{R}$, $\alpha_3, \eta \geq 0$ (by rescaling), $k_i \in \mathbb{Z}_+$, and $0 \leq \varepsilon_i \ll 1$; $i = 1, 2$. The corresponding system is

$$\dot{x} = y, \qquad \dot{y} = I_1 x - \eta x^2 - x^3 - \sum_{i=1}^{2} \varepsilon_i \frac{\partial f_i(x, I_1, I_2, k_i \theta_i)}{\partial x},$$

$$\dot{\theta}_1 = -\frac{x^2}{2} + \left(\frac{1}{2} + \alpha_1\right) I_1 + \alpha_3 I_2 + \sum_{i=1}^{2} \varepsilon_i \frac{\partial f_i(x, I_1, I_2, k_i \theta_i)}{\partial I_1}, \qquad \dot{I}_1 = -\varepsilon_1 \frac{\partial f_1(x, I_1, I_2, k_1 \theta_1)}{\partial \theta_1},$$

$$\dot{\theta}_2 = \alpha_2 + I_2 + \alpha_3 I_1 + \sum_{i=1}^{2} \varepsilon_i \frac{\partial f_i(x, I_1, I_2, k_i \theta_i)}{\partial I_2}, \qquad \dot{I}_2 = -\varepsilon_2 \frac{\partial f_2(x, I_1, I_2, k_2 \theta_2)}{\partial \theta_2}. \tag{8}$$

By construction, the unperturbed system ($\varepsilon_i = 0$) possesses at the origin, O_{xyI} ($O_{xyI} \equiv \{(x, y, I_1, I_2) | (x, y, I_1, I_2) = (0, 0, 0, 0)\}$), a 2D normally parabolic 1-resonant torus ($\dot{\theta}_1 = 0$ and the (x, y) subsystem has a zero eigenvalue there) for $\alpha_2 \neq 0$. For $\alpha_2 = 0$, O_{xyI} is a 2-resonant parabolic torus (in addition, $\dot{\theta}_2 = 0$ at the origin). More generally, $x = y = 0$ defines a four-dimensional invariant surface consisting of a family of 2-tori $O_{xy}(I) = \{(x, y, I_1, I_2) | x = y = 0\}$.

We assume that the phenomenological model is in the standard form for mechanical Hamiltonian systems which are integrable to quartic order, that the energy surfaces are compact in the (x, y) plane, and that the system undergoes a pitchfork bifurcation when the unfolding parameter η is set to zero. By a symplectic change of variables (for the integrable part of the Hamiltonian) only the first action, I_1, governs the stability type of the invariant 2-tori, while the other action, I_2, together with the external parameter, α_2, governs the existence of resonances. Hence, fixing $\eta \equiv 0$, for $I_1 < 0$ the 2-torus at $O_{xy}(I)$ is elliptic, for $I_1 = 0$ it is parabolic, and for $I_1 > 0$ it is hyperbolic. When $I_1 > 0$, additional two elliptic 2-tori, attached to the elliptic equilibria at $(x, y) = (\pm\sqrt{I_1}, 0)$ are created.

The system (8) is constructed such that for certain values of the parameters, listed below, some unperturbed energy surfaces contain a whole family of normally elliptic (or hyperbolic) resonant 2-tori emanating from a resonant parabolic torus. Then, the iso-energetic non-degeneracy condition fails on this family of tori and large instabilities of nearby perturbed orbits occur:

- When $\alpha_1 = 0$, the family of elliptic 2-tori $\{(x, y) = (\pm\sqrt{I_1}, 0); I_1 > 0, I_2 = 0\}$, which emanates from the parabolic torus at O_{xyI}, is iso-energetic and 1-resonant (creating a flat 1-PR).
- When $\alpha_2 = 0$ and $\alpha_1 = \alpha_3^2$ the family of 2-tori $\{(x, y) = (\pm\sqrt{I_1}, 0); I_1 \geq 0, I_2 = -\alpha_3 I_1\}$ is iso-energetic and 2-resonant; namely all tori are composed of fixed points (creating a flat 2-PR).
- When $\alpha_1 = -0.5$, the families of 1-resonant elliptic 2-tori $\{(x, y) = (0, 0); I_1 < 0, I_2 = 0\}$ and of 1-resonant hyperbolic 2-tori $\{(x, y) = (0, 0); I_1 > 0, I_2 = 0\}$ meet at the parabolic 1-resonant 2-torus at O_{xyI}, and are iso-energetic.
- When $\alpha_2 = 0$ and $\alpha_1 = \alpha_3^2 - 0.5$ the family of 2-tori $\{(x, y) = (0, 0); I_1 \in \mathbb{R}, I_2 = -\alpha_3 I_1\}$ is iso-energetic and 2-resonant (2-tori of mixed stability types, all consisting of fixed points).

Here we study in detail only the first two cases (see below).

The parameter η governs small asymmetric perturbations. When $\eta > 0$ and fixed, the system undergoes a saddle-center bifurcation and a transcritical bifurcation in I_1 (instead of the symmetric pitchfork bifurcation). For $I_1 < -\frac{1}{4}\eta^2$ the (x, y) system possess only one equilibrium, at the origin, which is elliptic. When $I_1 = -\frac{1}{4}\eta^2$ additional parabolic equilibrium at $(x, y) = (-\frac{1}{2}\eta, 0)$ is created. For $-\frac{1}{2}\eta^2 < I_1 < 0$ a center is created at $(x, y) = (\frac{1}{2}(-\eta - \sqrt{\eta^2 + 4I_1}), 0)$, and a saddle is created at $(x, y) = (\frac{1}{2}(-\eta + \sqrt{\eta^2 + 4I_1}), 0)$ (in addition to the elliptic equilibrium at the origin). When $I_1 = 0$, the equilibrium at $(x, y) = (\frac{1}{2}(-\eta + \sqrt{\eta^2 + 4I_1}), 0)$ coincides with the origin and becomes parabolic. And, when $I_1 > 0$, the origin becomes hyperbolic and $(x, y) = (\frac{1}{2}(-\eta + \sqrt{\eta^2 + 4I_1}), 0)$ becomes elliptic. All these equilibria of the (x, y) plane correspond to invariant 2-tori which are of the same normal stability type as the corresponding equilibrium. The appearance of transcritical bifurcation follows from fixing $O_{xy}(I)$ to be invariant for all I. Our preliminary study suggests that the system exhibits qualitatively different behavior for some values of $\eta > 0$. Here we treat only the symmetric case $\eta = 0$.

In Appendix A, we formulate the full set of conditions and assumptions from which we construct the phenomenological model. We stress that the ability to arrange a model which exhibits many types of PRs is not accidental—it follows from our results regarding the persistence/low co-dimensionality of these mechanisms of instabilities (see Section 4 for the corresponding theorems and [26,27] for the proofs).

Next, the global structure of the 3 d.o.f. system is described and in the following section numerical studies of the near-integrable system are presented.

2.1. The integrable system—bifurcation diagrams in the space of constants of motion

The classification of all the possible structures of the energy surfaces of integrable Hamiltonians is extremely challenging and has been completed for the 2 d.o.f. case only, see [7,15,22–24]. Some of these ideas have been extended to classify the integrable 3 d.o.f. dynamics of the Kovalevskaya top [11], the most complicated known example of an integrable 3 d.o.f. system.

To fully understand all possible behavior of the symmetric integrable 3 d.o.f. system (8) (i.e. system (8) with $\eta = 0$ and $\varepsilon = 0$), we construct bifurcation diagrams in the space of constants of motion. [7] Such diagrams reveal the critical energy levels and phase space regions in which strong instabilities arising from the perturbation are expected. In these diagrams the allowed regions of motion and the type of motion which occur are indicated. Different types of motion are necessarily divided by singular surfaces. Further information regarding the frequencies are inserted, with the understanding that these play a crucial role when the perturbation is applied.

Such an energy–momenta bifurcation diagram is presented in Fig. 1. The axes of the figure are the energy, H_0, and the actions of the 2-tori, I_2 and I_1 (more generally, the unperturbed Hamiltonian, where the full Hamiltonian is conserved under perturbation, and the conjugate actions to the resonant terms in the perturbed Hamiltonian). The solid curves in Fig. 1 correspond to normally elliptic invariant 2-tori; the dashed curves correspond to normally hyperbolic 2-tori (and their stable and unstable manifolds); the normally parabolic 2-tori reside at the meeting point between the solid and dashed curves, and are denoted by a circle ($\bigcirc$). Invariant 2-tori which are $(1, 0)$ resonant with respect to their inner frequencies (i.e. satisfy the resonance condition $\langle k, \omega \rangle = 0$ with $k = (1, 0)$) are denoted in Fig. 1 by an asterisk ($*$), and 2-tori which are $(0, 1)$ resonant denoted by lines of fat dots ($-\cdot-\cdot-$). The shaded region in this figure (light gray) corresponds to back-flow, i.e. to regions where the motion changes direction in θ_1, and where $(1, 0)$-resonance may occur (with respect to the inner frequencies of the 2-torus). Next we explain in detail the construction and the interpretation of such energy–momenta bifurcation diagrams, using Figs. 1–9 as illustrations.

---

[7] The relation of the Fomenko–Oshemkov graphs [15,31] to the energy–momenta bifurcation diagrams, which are developed here (and which were developed for 2 d.o.f. systems in [35]) and to the structures of the unperturbed energy surfaces in the three frequency space (see [26,27]), is the subject of current research.

$I2=-0.3:0.02:0.3, \alpha 1=0.3, \alpha 2=0.2, \alpha 3=1$
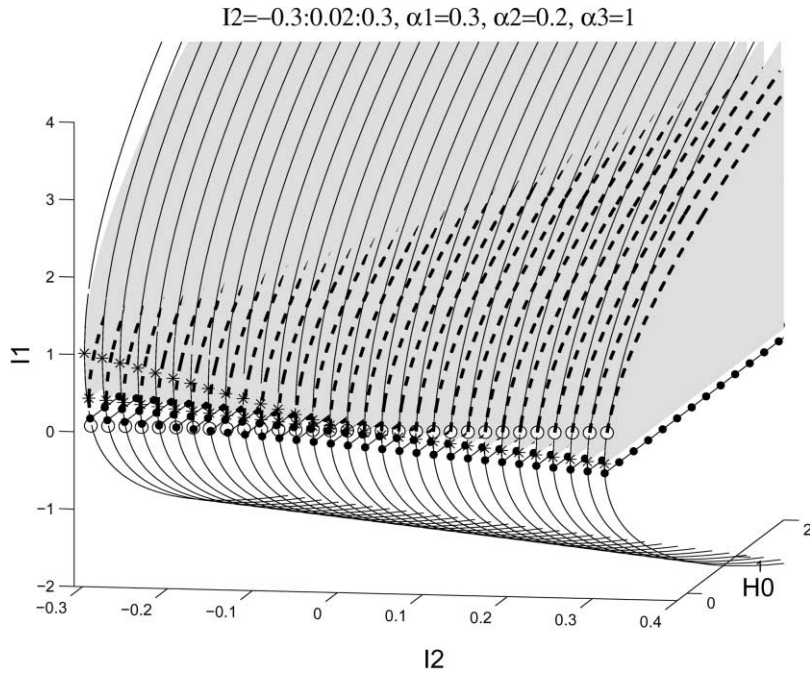
Fig. 1. Energy–momenta bifurcation diagram. Elliptic 2-tori (---); hyperbolic 2-tori (and separatrices) (−−−); parabolic 2-tori (○○○); resonances (∗ ∗ ∗ and –·–·–); back-flow (shaded volume).
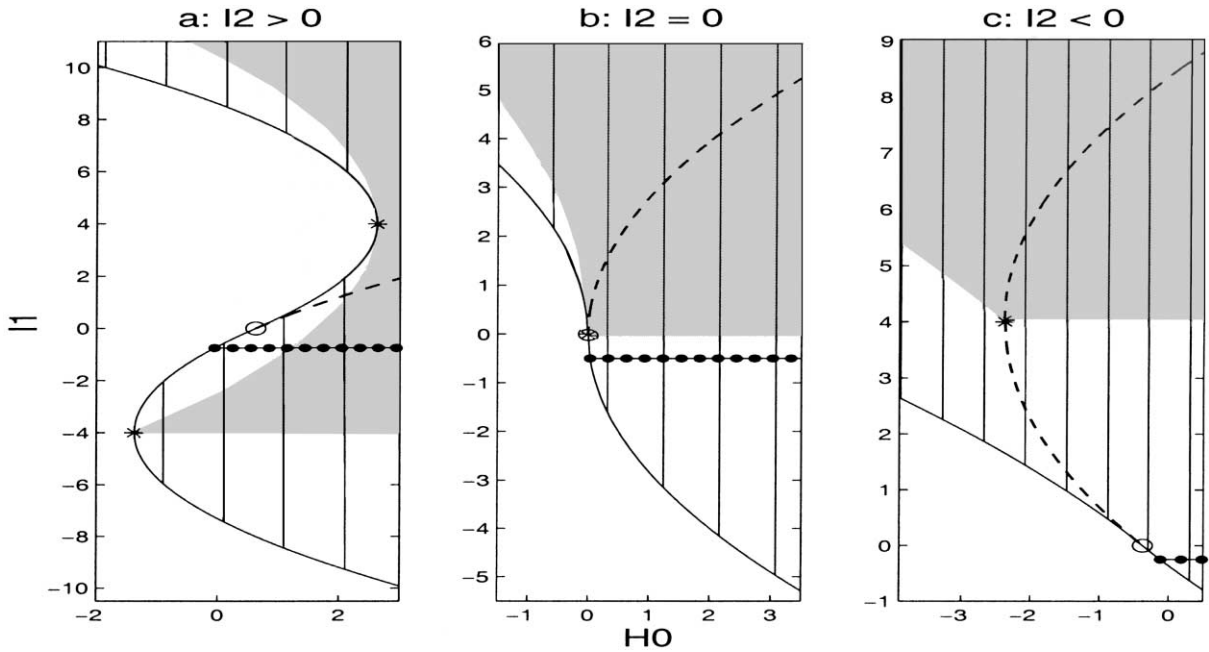
Fig. 2. Slices of the energy–momenta bifurcation diagram for $\alpha_1 < 0$. $\alpha_1 = -0.25$, $\alpha_2 = 1$, $\alpha_3 = 2$. (a) $I_2 = 0.5$; (b) $I_2 = 0$; (c) $I_2 = -0.5$.
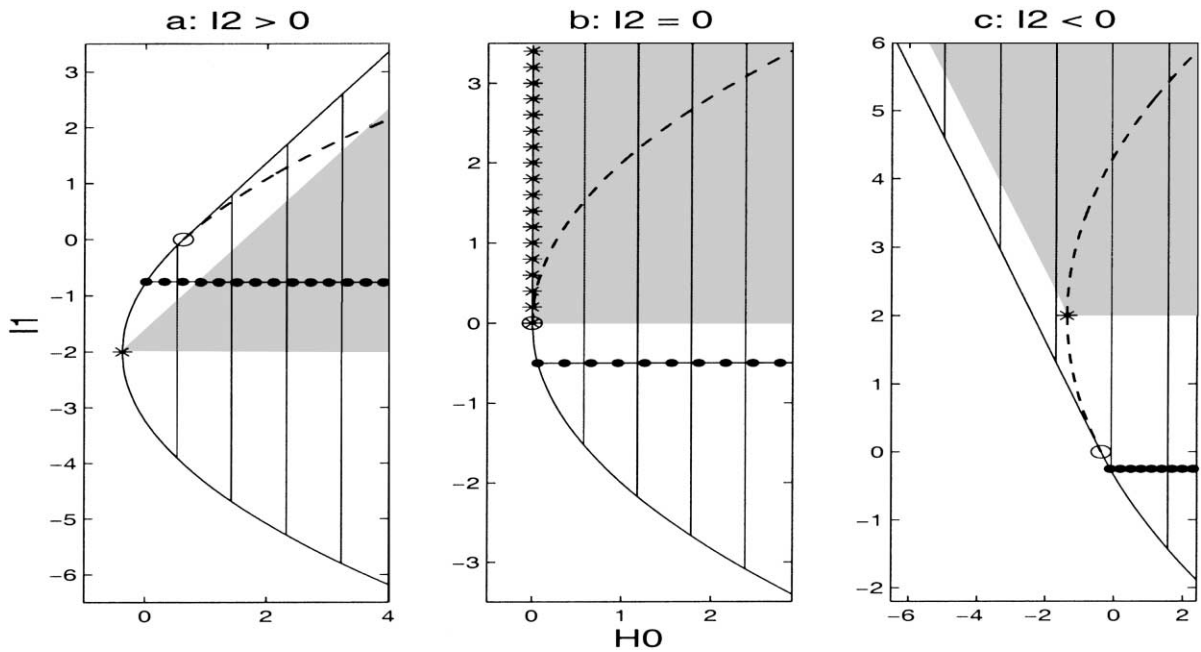
Fig. 3. Slices of the energy–momenta bifurcation diagram for $\alpha_1 = 0$. $\alpha_1 = 0$, $\alpha_2 = 1$, $\alpha_3 = 2$. (a) $I_2 = 0.5$; (b) $I_2 = 0$; (c) $I_2 = -0.5$.
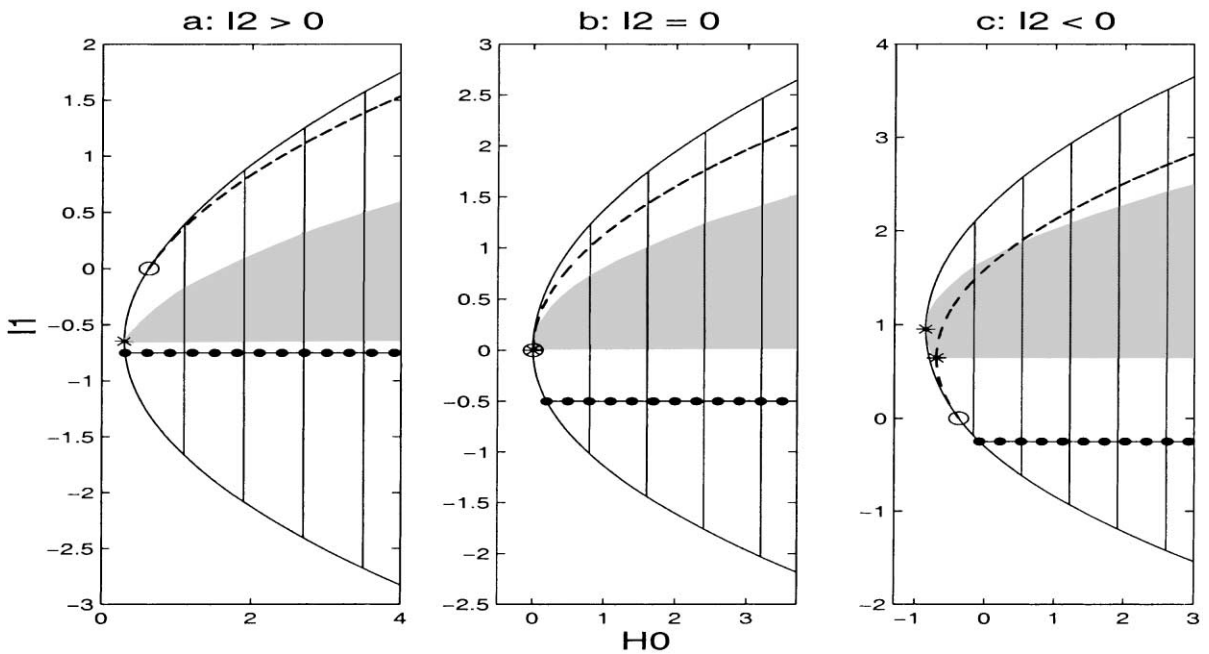
Fig. 4. Slices of the energy–momenta bifurcation diagram for $\alpha_1 > 0$. $\alpha_1 = 1.05$, $\alpha_2 = 1$, $\alpha_3 = 2$. (a) $I_2 = 0.5$; (b) $I_2 = 0$; (c) $I_2 = -0.5$. Regions of allowed motion (vertical lines); elliptic 2-tori (—); hyperbolic 2-tori (and separatrices) (– – –); parabolic 2-tori (○); resonances (∗∗ and –·–·–); backflow (shaded volume).
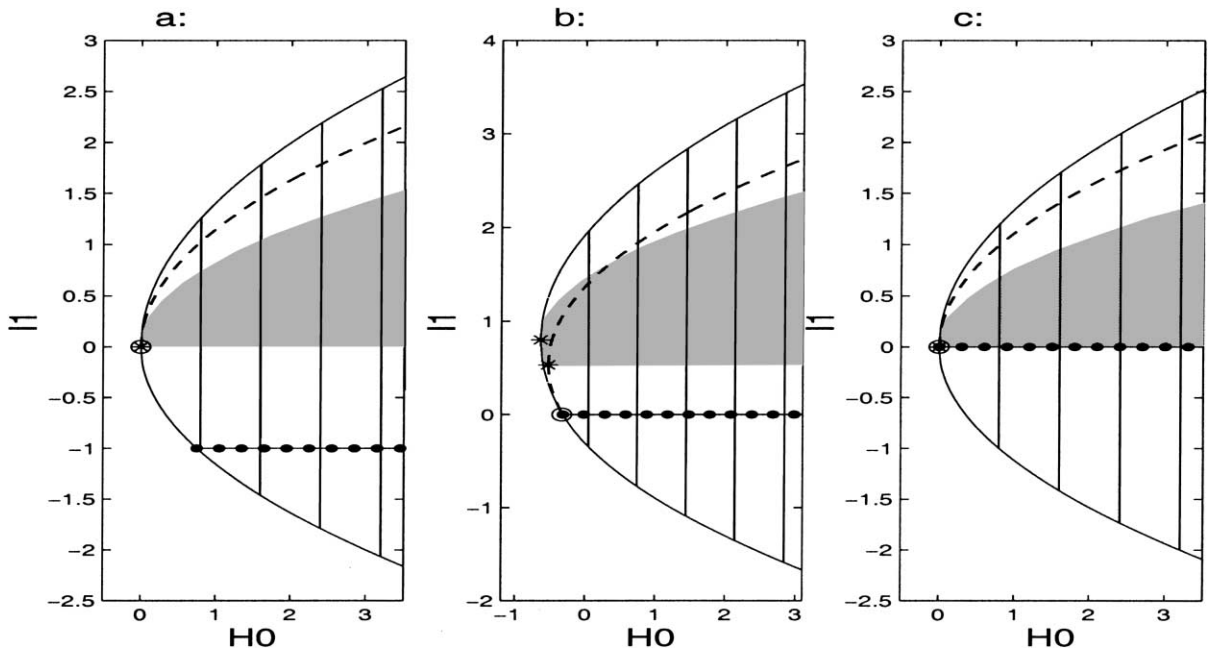
Fig. 5. Slices of the energy–momenta bifurcation diagrams at PRs with $\alpha_1 > 0$. $\alpha_1 = 1.05$, $\alpha_3 = 2$. (a) $I_2 = 0, \alpha_2 = 1$: parabolic 1-resonance in the direction of I_1 ($\{(1, 0, 0), (0, 1, 0)\}$-resonance); (b) $I_2 = -\alpha_2 = -1$: parabolic 1-resonance in the direction of I_2 ($\{(1, 0, 0), (0, 0, 1)\}$-resonance); (c) $I_2 = \alpha_2 = 0$: parabolic 2-resonance ($\{(1, 0, 0), (0, 1, 0), (0, 0, 1)\}$-resonance).
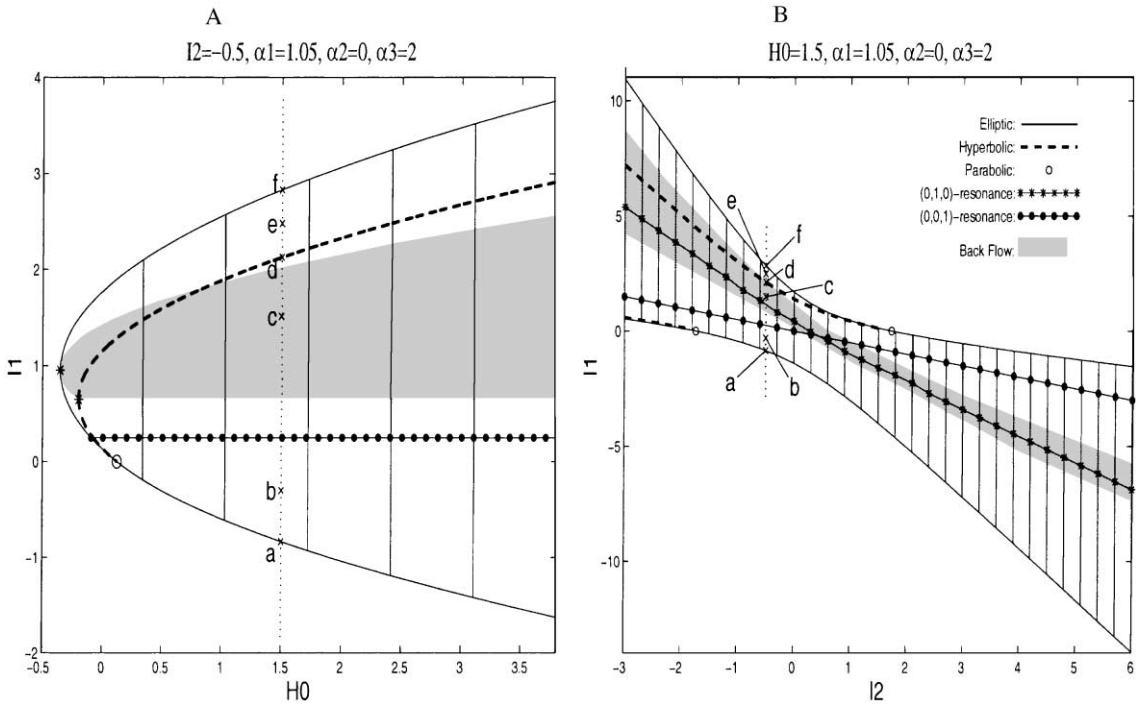
Fig. 6. 2D slices of the 3D energy–momentum bifurcation diagram. (A) $I_2 = -0.5$; (B) $H_0 = 1.5$.
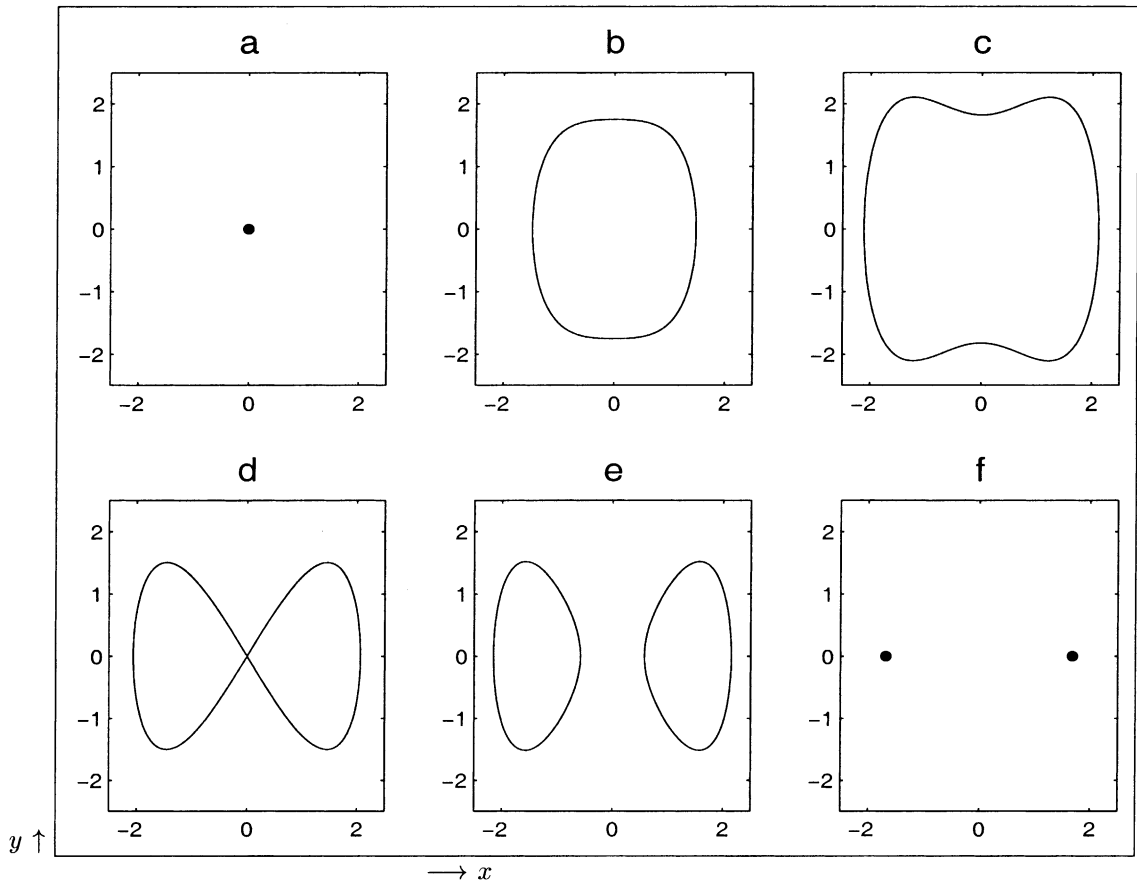
Fig. 7. Orbit structure in the (x, y) plane. $H_0 = 1.5$, $I_2 = 0.5$, and I_1 values at subfigures (a)–(f) are as indicated in Fig. 6; $\alpha_1 = 1.05$, $\alpha_2 = 0$, $\alpha_3 = 2$.

The regions in the *space of constants of motion*, (H_0, I), where motion is allowed for the integrable system (8) ($\varepsilon_i = 0$) are determined by analyzing the Hamiltonian (5), and determining its domain of definition (see below and Appendix B for details). A regular point in the allowed region of motion corresponds to one or two 3-tori; e.g. any inner point with respect to the solid curves (horizontal parabolas) in the energy–momenta bifurcation diagram in Fig. 1 is such a regular point. As the Hamiltonian (5) is in normal coordinates form, a singular point of the (x, y) plane corresponds to an isolated invariant 2-torus, with the same normal stability type as of the (x, y) equilibria. The singular surfaces corresponding to the stable (elliptic) equilibria of the (x, y) plane are denoted by a manifold of solid curves in Fig. 1, where each curve corresponds to a fixed value of I_2. In our representation, elliptic equilibria in the (x, y) plane supply the boundaries to the energy surfaces of the full system (it follows from [4, p. 102]). Hence, these singular surfaces of normally elliptic 2-tori supply the boundary of the allowed region of motion. To find these boundaries, Eq. (5) is solved at these equilibria points for the first action, I_1, as a function of the other two constants of motion, H_0 and I_2; the detailed calculations appear in Appendix B. The result of these calculations are the location of the equilibria manifolds (which depend non-trivially on the parameters, see Appendix B). For the parameter values of Fig. 1, the upper bounding manifold is given by the
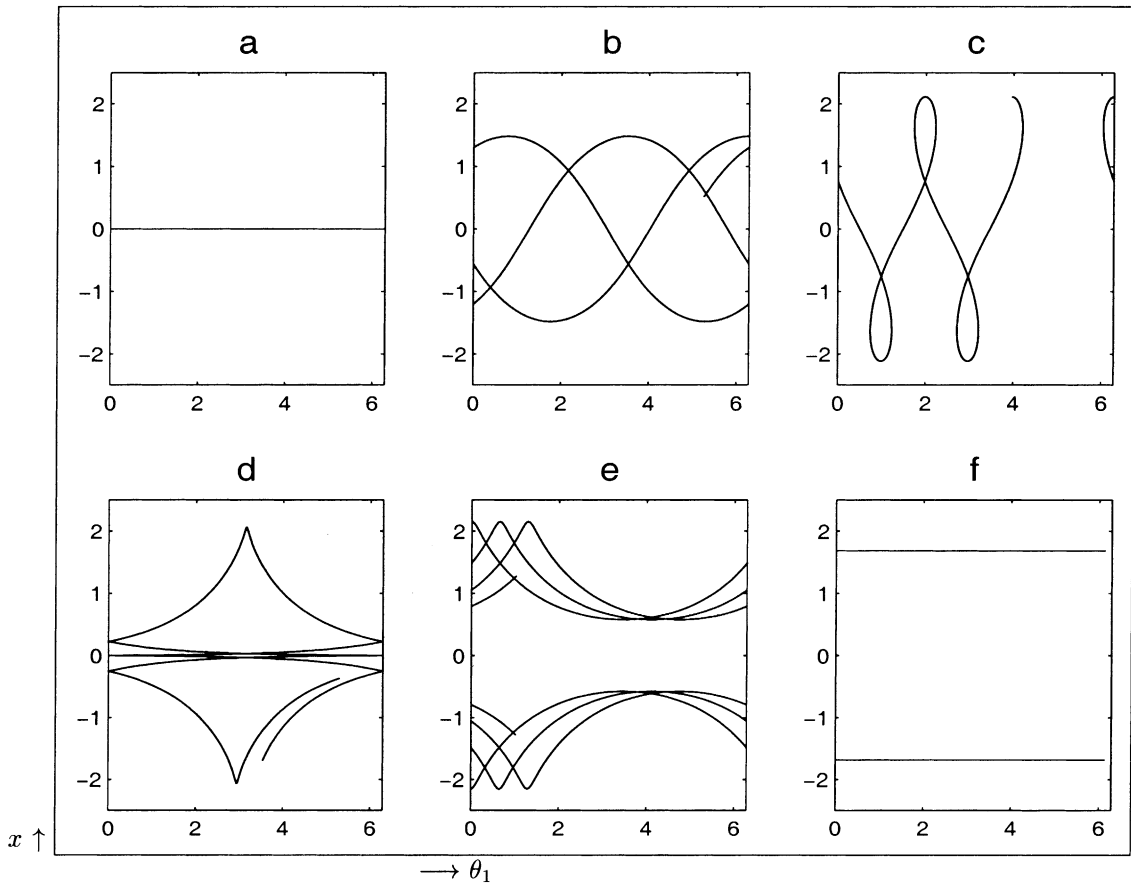
Fig. 8. Orbit structure in the (θ_1, x) plane. $H_0 = 1.5$, $I_2 = 0.5$, and I_1 values at subfigures (a)–(f) are as indicated in Fig. 6; $\alpha_1 = 1.05$, $\alpha_2 = 0$, $\alpha_3 = 2$. (c) Back-flow.

equation

$$I_{1_{\mathrm{ell}\pm}}(H_0, I_2) = \frac{-\alpha_3 I_2 \pm \sqrt{I_2^2(\alpha_3^2 - \alpha_1) - 2\alpha_1\alpha_2 I_2 + 2\alpha_1 H_0}}{\alpha_1}, \tag{9}$$

for values of H_0 and I_2 such that $I_{1_{\mathrm{ell}\pm}}(H_0, I_2) \geq 0$, and the lower bounding manifold is given by

$$I_{1_{O_{xy}\pm}}(H_0, I_2) = \frac{-2\alpha_3 I_2 \pm 2\sqrt{\alpha_3^2 I_2^2 - (1 + 2\alpha_1)(\alpha_2 I_2 + (I_2^2/2) - H_0)}}{1 + 2\alpha_1} \tag{10}$$

for values of H_0 and I_2 such that $I_{1_{O_{xy}\pm}}(H_0, I_2) \leq 0$. The singular surface corresponding to the unstable (hyperbolic) equilibria at the origin of the (x, y) plane, O_{xy}, and *separatrices*, are denoted by a manifold of dashed curves, each corresponding to a fixed value of I_2. The manifold of dashed curves in Fig. 1 is given by Eq. (10) for values of H_0 and I_2 such that $I_{1_{O_{xy}\pm}}(H_0, I_2) > 0$.

Above the manifold of dashed curves each regular point corresponds to a pair of 3-tori (corresponding, in the (x, y) plane, to the right and left periodic orbits residing inside the figure eight separatrix), whereas below it only one 3-torus is associated with each (H_0, I) value (corresponding to orbits which encircle the origin in the (x, y)
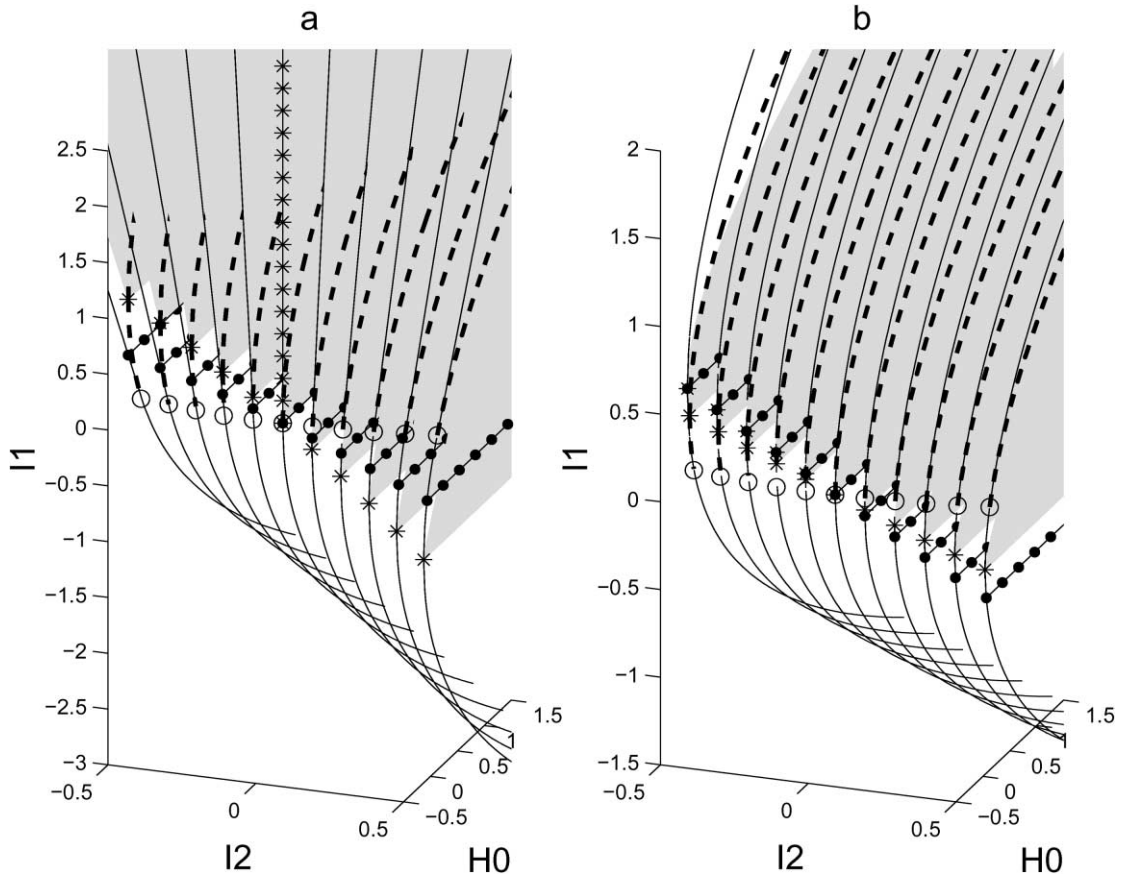
Fig. 9. Two types of flat PRs. $\alpha_2 = 0$, $\alpha_3 = 1$. (a) $\alpha_1 = 0$, $I_2 = -0.5{:}0.05{:}0.5$; (b) $\alpha_1 = \alpha_3^2 = 1$, $I_2 = -0.5{:}0.05{:}0.5$.

plane). Hence, the normally hyperbolic 2-tori create a topological non-trivial deformation of the energy surface. Beginning at the manifold of dashed curves, the energy surface branches, so that its upper boundary is composed of two manifolds of elliptic 2-tori (at $(x, y) = (\pm\sqrt{I_1}, 0)$). These are denoted by solid curves in the figures, and here, by symmetry, they are identified (for $\eta \neq 0$, two upper solid curves will appear in the figure). The boundary between the solid and dashed surfaces, which is denoted by a line of circles ($\bigcirc$), corresponds to the parabolic 2-tori. Notice that each parabolic torus in Fig. 1 resides on a different energy surface.

We have thus demonstrated how the normal stability of the lower dimensional tori are represented in the diagram. In Figs. 2–6 the domains of definition of Eq. (5) is shown by vertical lines. [8]

Figs. 2–4, in which 2D slices of energy–momenta bifurcation diagrams—each corresponding to a fixed value of I_2, demonstrate the dependence of the bounding curves and the regions of allowed motion on the parameters and constants of motion (H_0, I). For our model (the integrable Hamiltonian (5) and system (8)) we observe a wide variety of possibilities for such dependence (see Appendix B for details). In particular, for a fixed I_2, the energy surfaces are always bounded from below in I_1 direction by an elliptic 2-torus; when $-0.5 < \alpha_1 < 0$ the motion is

---

[8] In the three-dimensional (3D) bifurcation diagram in Fig. 1 the vertical lines were omitted for the convenience of the viewer, and the domain where motion is allowed in this figure is inside the parabola created by the upper and lower manifolds of solid curves (which refer to the elliptic equilibria points in the (x, y) plane).

unbounded from above in I_1 direction for any value of I_2 (see e.g. Fig. 2), and when $\alpha_1 = 0$ the motion is unbounded from above for $I_2 \leq 0$ (see e.g. Fig. 3b and c). In all the other cases motion is bounded from above in I_1 direction by an elliptic 2-torus (see Figs. 1, 3a and 4). *Hence, in some cases there is no bound on the growth of the actions.*

The above procedure reveals all the possible topological distinct types of integrable level sets and their stability. Clearly, for a fixed energy value, h, the perturbed orbits reside on the energy surface $H(x, y, \theta, I) = h$, hence a complete understanding of this energy surface geometry supplies bounds on the instability rates of the actions. However, generally, plotting this surface is complicated—it is a five-dimensional surface (for 3 d.o.f. systems), and its projection to the I variables plane is different for each value of θ. Hence, one wants to conclude regarding the instability range from the corresponding $H_0(x, y, I) = h_0$ plots, or more precisely, from the unperturbed energy–momenta bifurcation diagrams. Indeed, consider the following band of unperturbed surfaces:

$$H_{\text{band}} = \{(x, y, I) | |H_0(x, y, I) - h| < K(\varepsilon_1 + \varepsilon_2)\}, \quad K = \text{constant}, \tag{11}$$

and let

$$I^{\min} = \inf_{I \in H_{\text{band}}} I, \qquad I^{\max} = \sup_{I \in H_{\text{band}}} I.$$

Then, since we assumed that the perturbation is small in the C^r topology, it follows that for the perturbed orbits, $I \in [I^{\min}, I^{\max}]$ for all time. Namely, if these bounds are finite, we obtain *a priori bounds on the extent of the instability in the actions*. Furthermore, in case one of the angles, say θ_2, is rapidly rotating, the corresponding action I_2 is approximately conserved (i.e. conserved for a long time). Then, define the section of H_{band}

$$\bar{H}_{\text{band}}(\bar{I}_2) = \{(x, y, I) | I_2 = \bar{I}_2, \ |H_0(x, y, I) - h| < K(\varepsilon_1 + \varepsilon_2)\}, \tag{12}$$

and the conditional lower and upper bounds in the I_1 direction may be similarly found

$$\bar{I}_1^{\min}(\bar{I}_2) = \inf_{I_1 \in \bar{H}_{\text{band}}(\bar{I}_2)} I_1, \qquad \bar{I}_1^{\max}(\bar{I}_2) = \sup_{I_1 \in \bar{H}_{\text{band}}(\bar{I}_2)} I_1.$$

Indeed, these bounds can be explicitly calculated using Eq. (11); see Fig. 17 for demonstration of their effect (see also [26,27]).

Next we consider the frequency vectors of the integrable system (8) ($\varepsilon_i = 0$) and the appearance of resonances. Each point in the space of constants of motion, (H_0, I), has a frequency vector of the form

$$(\omega_0, \omega_1, \omega_2) = (\omega_0(H_0, I), \omega(H_0, I)), \tag{13}$$

representing the motion in the (x, y) plane, and the (θ, I) planes, respectively. At regular points of the space (H_0, I), $\omega_0(H_0, I)$ is just the first inner frequency of the corresponding 3-torus. A singular point of the (x, y) plane corresponds to an invariant 2-torus, with a 2D vector of inner frequencies, $\omega(H_0, I) = (\omega_1, \omega_2) = (\dot{\theta}_1(I), \dot{\theta}_2(I))$; the normally elliptic and parabolic invariant 2-tori have in addition a normal frequency, $\omega_0 = \Omega(I)$, while for normally hyperbolic 2-tori the normal frequency (and hence ω_0) cease to exist. To obtain a continuous dependence on (H_0, I) we formally define ω_0 to be zero at such points

$$\omega_0(H_0, I) = \begin{cases} \Omega(I), & \{(x, y) = (0, 0), I_1 \leq 0\}, \{(x, y) = (\pm\sqrt{I_1}, 0), I_1 \geq 0\}, \\ 0, & \{(x, y) = (0, 0), I_1 > 0\}, \\ \dfrac{2\pi}{T(H_0, I)}, & \text{Otherwise}, \end{cases} \tag{14}$$

where $T(H_0, I)$ is the period of the corresponding (x, y) orbit(s). See for illustration Fig. 6A (a 2D slice of an energy–momenta bifurcation diagram with a fixed value of $I_2 = -0.5$) and Fig. 7 (the corresponding motion in the (x, y) plane at six different points along the line $\{H_0 = 1.5, I_1\}$): (a) and (f) correspond to elliptic 2-tori

with $\omega_0(I) = \Omega(I) \neq 0$ (at a parabolic 2-torus $\omega_0(I) = \Omega(I_1 = 0, I_2) = 0$); (d) corresponds to a hyperbolic 2-torus and its stable and unstable manifolds where $\omega_0(H_0, I) \to 0$; (b), (c) and (e) correspond to 3-tori with $\omega_0(H_0, I) = 2\pi/T(H_0, I)$, where $T(H_0, I)$ is the period of the corresponding periodic (x, y) orbits shown in Fig. 7. Figs. 6–8 are explained in more detail below.

Generally, resonances $\langle k, (\omega_0, \omega) \rangle = 0; k \in \mathbb{Z}^3 \setminus \{0\}$ appear in the 3D energy–momenta bifurcation diagrams as 2D surfaces, intersecting each energy level by a curve. A full set of these curves creates a resonance web on each energy surface (see e.g. [3,25] and references therein). Resonance surface information, for resonances of the maximal dimensional 3-tori, may be added to these diagrams by averaging along the motion in the (x, y) plane to compute the frequencies ω_0 and ω_1 (ω_2 is simply $\dot{\theta}_2(I) = \alpha_2 + I_2 + \alpha_3 I_1, \forall x, y \in \mathbb{R}$). An example of such a resonance curve, corresponding to vanishing of ω_1 on 3-tori of one fixed energy surface, is presented in Fig. 6B as a line of asterisks. Special resonances may be directly found, and are denoted in the following way on the bifurcation diagrams in Figs. 1–5, 6A and 9: the $k = (0, 0, 1)$-resonances, corresponding to vanishing of the frequency in the I_2 direction ($\omega_2 = \dot{\theta}_2(I) = 0$) are marked by lines of fat dots on each 2D slice with a fixed value of I_2, and by a surface of dotted lines on the 3D diagrams; the $(0, 1, 0)$-resonance surface, corresponding to vanishing of the frequency in the direction of I_1, intersects the singular surfaces of invariant 2-tori in the 3D diagrams (Figs. 1 and 9) at the curve of asterisks (on which $\omega_1 = \dot{\theta}_1(I) = 0$), and it is denoted by a single asterisk on the 2D slices. For example, in Fig. 1 it is seen that the line of circles, corresponding to the normally parabolic 2-tori ($I_1 = 0$) is crossed by the $(0, 1, 0)$-resonance curve of asterisks (only) at $I_2 = 0$, and by the $(0, 0, 1)$-resonance surface of dotted lines (only) at $I_2 = -\alpha_2 = -0.2$. All other resonant parabolic tori in Fig. 1 have weaker resonances (larger $|k|$ values) with respect to their *inner frequencies*. In Fig. 5, we show 2D slices of bifurcation diagrams where parabolic resonant 2-tori are recorded.

As the normal frequency, $\omega_0 = \Omega$, vanishes on normally parabolic tori, normally parabolic tori are a priori $(1, 0, 0)$-resonant. Hence, when the $(0, 1, 0)$-resonance surface intersects a parabolic 2-torus, it corresponds to occurrence of the *double* $\{(1, 0, 0), (0, 1, 0)\}$-resonance (see Fig. 5a), and when the $(0, 0, 1)$-resonance surface intersects a parabolic 2-torus, it corresponds to occurrence of the *double* $\{(1, 0, 0), (0, 0, 1)\}$-resonance (see Fig. 5b). When $\alpha_2 = 0$, the curve of asterisks, the surface of dotted lines and the line of circles all intersect at one point, corresponding to a 2-resonant normally parabolic torus, an event which corresponds to occurrence of the *triple* $\{(1, 0, 0), (0, 1, 0), (0, 0, 1)\}$-resonance. This event may be seen, e.g., in Fig. 5c and Fig. 9. Therefore, the instabilities in the near-integrable system (described in the following sections), which are a result of PRs, correspond to cross resonance diffusion. [9] See [26,27] for more details and a discussion on the place and role of parabolic resonant tori in the resonance web.

Another dynamical feature of interest is the possible existence of a back-flow in θ_1, namely a non-monotonic dependence of θ_1 on t, see Fig. 8c. The regions where $\dot{\theta}_1$ changes sign along orbits are colored by a light gray in the bifurcation diagrams (see Figs. 1, 2, 4, 6 and 9). Such a dynamical feature (detecting instantaneous zeroes of $\dot{\theta}_1$) may be found easily (see Appendix C and Table 2). The significance of this region is three-folded. First, only in a region where back-flow occurs the inner frequency ω_1 may vanish (equivalently, a $(0, 1, 0)$-resonance may appear; e.g. see the curve of asterisks in the light gray area of Fig. 6B). Second, when a back-flow occurs along a separatrix the usual transport mechanism associated with separatrix splitting must be modified. This scenario appears when the light grey shaded region in the energy–momenta bifurcation diagrams covers the dashed hyperbolic equilibria curve. Finally, when $\dot{\theta}_1$ vanishes identically on a lower dimensional invariant torus ($\omega_1 = \dot{\theta}_1 = 0$), a $(1, 0)$-resonance occurs with respect to the *inner frequencies* of the 2-torus. Hence, the intersection of the light grey volume with the (x, y) equilibria surfaces consists of resonant 2-tori which are indicated by asterisks in Figs. 1–5, 6A and 9.

The singular surfaces of 2-tori and the phase information encoded in the bifurcation diagram allows one to extract complete description of the integrable motion. For clarity, by fixing I_2, we present isolated 2D slices of the 3D

---

[9] See [17] and references therein for cross resonance diffusion near hyperbolic double resonances.

bifurcation diagrams in the energy–momenta space in Figs. 2–5 and 6A (the vertical solid lines in these figures denote the region of allowed motion).

Figs. 6–8 illustrate the different structures of orbits of the integrable part of system (8). Consider Fig. 6A, in this figure we present a slice of a bifurcation diagram with a fixed value of $I_2 = -0.5$. The energy surface with energy value $H_0 = 1.5$ intersects this diagram at the light vertical dotted line. Alternatively, a slice of the bifurcation diagram in the (I_2, I_1) plane at the corresponding energy value $H_0 = 1.5$, is presented in Fig. 6B, where the corresponding light dotted vertical line denotes the intersection with the slice $I_2 = -0.5$. The points denoted by (a), (b), (c), (d), (e) and (f) on these two light dotted vertical lines correspond to the six different types of orbits appearing on the energy surface with $H_0 = 1.5$ at $I_2 = -0.5$. The corresponding six different types of motion in the (x, y) and (θ_1, x) planes are presented in Figs. 7 and 8, respectively. The point (a) corresponds to one elliptic equilibrium in the (x, y) plane, hence to one normally elliptic 2-torus in the six-dimensional phase space; the point (b) corresponds to a periodic orbit in the (x, y) plane (hence to a non-resonant 3-torus, which is densely covered by this orbit), which encircles the origin, and on which $\dot{\theta}_1$ does not change sign (since it is located in an unshaded region); the point (c) is in the shaded region hence it corresponds to a larger periodic orbit which encircles the origin in the (x, y) plane and exhibits back-flow in θ_1 (topologically it is indistinguishable from (b), yet see Fig. 8c); the point (d) corresponds to an hyperbolic equilibrium and its separatrix in the (x, y) plane, hence to an invariant normally hyperbolic 2-torus and its corresponding 3D stable and unstable manifolds; the point (e) corresponds to two 3-tori, and the point (f) corresponds to two isolated invariant normally elliptic 2-tori. The motion for initial conditions with different energies and actions can be now read-off from Fig. 6 or its 3D extension.

We regress to supply a few more details regarding the appearance of strong resonances. In particular, we demonstrate that *geometrical features of the bifurcation diagram have dynamical significance*.

In the integrable system (8), $\dot{\theta}_1$ vanishes on a lower dimensional invariant torus in two cases. The first case occurs when

$$\omega_1|_{O_{xy}} = \dot{\theta}_1|_{O_{xy}} = \left.\frac{\partial H_0}{\partial I_1}\right|_{(x,y)=(0,0)} = 0. \tag{15}$$

Graphically, this means that the resonance occurs exactly at the fold of the surface in the I_1 direction. In other words, for any fixed I_2, the I_1 which solves (15) is a local extrema of the energy value of the equilibria curves, see Figs. 1–5, 6A and 9. It can be easily verified that this observation is correct even when the equilibria position depends on the actions.[10] These resonant lower dimensional tori are indicated by an asterisk in the bifurcation diagrams in Figs. 1–5, 6A and 9.

Eq. (15) holds for

$$I_{2_{\text{res1}}}(I_1) = -\frac{1 + 2\alpha_1}{2\alpha_3} I_1 \tag{16}$$

for any value of I_1. Hence, the corresponding resonant tori may be of any stability type, depending on the value of I_1. In particular, since $I_{2_{\text{res1}}}(0) = 0$, the $(0, 1, 0)$-resonant 2-torus at O_{xyI} is normally parabolic, and is therefore indicated by both asterisk and a circle in Fig. 5a. In Section 2.2 this parabolic 1-resonance is referred to as 1-PR in I_1 direction.

The second case occurs when

$$\omega_1|_{\text{ell}} = \dot{\theta}_1|_{\text{ell}} = \left.\frac{\partial H_0}{\partial I_1}\right|_{(x,y)=(\pm\sqrt{I_1},0)} = 0. \tag{17}$$

---

[10] For example, defining $G(I) = H_0(x(I), y(I), I)$, where $(x(I), y(I))$ are the equilibrium solution, we see that $\partial G/\partial I_1 = \partial H_0/\partial I_1|_{(x(I),y(I),I)}$ because $\nabla_{xy}H_0|_{(x(I),y(I),I)} = 0$.

Namely, when the elliptic equilibria surface corresponding to $(x, y) = (\pm\sqrt{I_1}, 0)$ folds in the I_1 direction. Eq. (17) holds for

$$I_{2_{\text{ell-res}}}(I_1) = -\frac{\alpha_1}{\alpha_3} I_1 \tag{18}$$

for positive values of I_1 and corresponds to two $(0, 1, 0)$ 1-resonant 2-tori which are normally elliptic. It follows that when α_1/α_3 is positive (negative) the bounding equilibria surface folds to the right (left), hence $H_{0_{\text{ell-min}}}$ corresponds to the minimal (maximal) energy value for which the equilibria curves (Eq. (9)) corresponding to $(x, y) = (\pm\sqrt{I_1}, 0)$ are defined, see Fig. 4c (Fig. 2a). Note that for non-positive α_1 the PR scenario results in a fundamental change of the energy surface properties—from being locally bounded in I_1 direction near the resonance for, say $I_2 > 0$, to being locally unbounded there for $I_2 \leq 0$.

Since $\dot\theta_2$ does not depend on the (x, y) variables (see Eqs. (8)), when $\omega_2 = \dot\theta_2$ vanishes a $(0, 0, 1)$-resonance occurs. This is indicated in Figs. 1 and 9 by a surface of dotted lines and in Figs. 2–6 by lines of fat dots. In the integrable system (8), $\dot\theta_2$ vanishes identically when

$$\omega_2 = \dot\theta_2 = \frac{\partial H_0}{\partial I_2} = 0. \tag{19}$$

Namely when the energy surface has a fold in the I_2 direction. Eq. (19) holds for

$$I_{2_{\text{res2}}}(I_1) = -\alpha_2 - \alpha_3 I_1. \tag{20}$$

In Fig. 5b, the line of fat dots, which corresponds in this figure to $I_2 = I_{2_{\text{res2}}}(0) = -\alpha_2$, intersects the circle ($\bigcirc$), which marks the parabolic torus. In Section 2.2, the corresponding 1-PR that occurs in the near-integrable system is referred to as 1-PR in I_2 direction. We emphasize that in Figs. 1 and 9 the grey volume corresponds to the existence of instantaneous zeroes of $\dot\theta_1$, which possibly contain a resonance surface on which $\omega_1 = 0$; the 2D surfaces of dotted lines in these figures correspond to real resonance in the I_2 direction, namely $\omega_2 = 0$.

We see that these bifurcation diagrams enable one to summarize the global structure of an integrable system for all its energy levels. It is seen that critical energy levels may be easily identified (e.g. in Fig. 5a–c there exist (slices of) energy surfaces (in I_2) for which PRs exist—see Figs. 10, 12 and 14, respectively, for the corresponding dynamics in the near-integrable system), and bifurcations induced by external parameters result in qualitative changes in these diagrams (e.g. compare Figs. 2–4). Furthermore, under small perturbation the Hamiltonian is preserved and the sources of instability for any given energy level are explicitly visible in the diagram.

We are now in position to identify possible sources of substantial instabilities in the near-integrable system (8). As described below, these events depend on the parameters α_1, α_2 and α_3.

When $\dot\theta_1$ and $\dot\theta_2$ of the integrable part of system (8) vanish simultaneously on an invariant 2-torus, two independent resonance conditions are met, and a double resonance (a 2-resonance with respect to the inner frequencies of the 2-torus) occur in the near-integrable system. When the parameter $\alpha_2 = 0$ (for any non-zero values of the other parameters in the system), this event occurs at O_{xyI}, and a 2-PR takes place in the near-integrable system. Appearance of a normally parabolic 2-resonant torus on a certain energy surface may be seen in Fig. 5c. In this figure an energy–momentum bifurcation diagram in which Eqs. (16) and (20) hold simultaneously at the parabolic torus is presented. In this case the integrable system exhibits a *triple resonance* with respect to the corresponding 3-frequency vector, $(\omega_0, \omega_1, \omega_2)$, and the near-integrable system exhibits large instabilities (2-PR), as described in Section 2.2.

When the parameter $\alpha_1 = 0$ (for any non-zero values of the other parameters in the system), it follows from Eq. (18) that $I_{2_{\text{ell-res}}}(I_1) \equiv 0$ for any non-negative value of I_1. Hence, a whole family of elliptic 1-resonant tori (a vertical line of asterisks in Fig. 3b and Fig. 9a), together with a *parabolic* resonant torus at the origin, reside on the same energy surface $H_0 = 0$. Furthermore, this energy surface is unbounded in the positive direction of I_1

(see Fig. 3b and Fig. 9a). This scenario induces a flat 1-PR in the near-integrable system, leading to order one instabilities in I_1 of nearby initial conditions. *Such large instabilities in I_1 are possible as the energy surface is unbounded in its positive direction.* When $\alpha_1 > 0$ but small, the energy surface is large in I_1, but still bounded, and perturbed orbits are seen to reach the boundaries of such energy surfaces (see e.g. Fig. 11).

When $\alpha_1 = \alpha_3^2 \neq 0$ and $\alpha_2 = 0$, from Eqs. (18) and (20) it follows that $I_{2_{\text{ell-res}}}(I_1) = I_{2_{\text{res2}}}(I_1) = -\alpha_3 I_1$ for any non-negative value of I_1. Hence, for these parameter values, a whole family of 2-resonant elliptic tori (for positive values of I_1) together with a *parabolic* 2-resonant torus (corresponds to vanishing of I_1) reside on the same unbounded energy surface of the integrable system along the line $I_2 = -\alpha_3 I_1$, see Fig. 9b (in this figure $\alpha_1 = \alpha_3^2 = 1$ and the energy surface $H_0 = 0$ contains a whole family of 2-resonant 2-tori of mixed stability types and is unbounded in the direction $I_1 = -I_2$). Indeed, a flat 2-PR occurs in the perturbed system on nearby energy surfaces, and very large (order 1) instabilities are observed in numerical experiments in the positive direction of I_1 and in the negative direction of I_2.

Summarizing, when the energy surface of the integrable system is unbounded in the direction of a resonance at the parabolic lower dimensional torus, then a degenerate scenario occurs, by which a whole family of resonant tori of mixed stability types (hence containing the parabolic resonant torus) reside on the same energy surface. In particular, this happens in the system (8) when $\dot{\theta}_1$ vanishes for a whole range of $I_1 \geq 0$ values. Since (5) includes only terms up to quadratic order in I_1, we can arrange such scenarios by varying one or two parameters. In Fig. 3b and Fig. 9b we present such situations, where a line of asterisks is seen to cover a whole line of I_1 values. In the generic case this situation is of infinite co-dimension; tangential PRs, which are the first approximation to the flat PRs are a low co-dimension (one or two) phenomena for 3 d.o.f. systems (see [26,27] [11]).

In Section 2.2, we describe the corresponding scenarios in the near-integrable system.

2.2. The near-integrable system

For near-integrable 3 d.o.f. Hamiltonian systems there are three possible types of PR:

Case 1: Parabolic 1-resonance in I_1 direction ($\dot{\theta}_1 = 0$ in the integrable system (8), Fig. 5a).
Case 2: Parabolic 1-resonance in I_2 direction ($\dot{\theta}_2 = 0$ in the integrable system (8), Fig. 5b).
Case 3: Parabolic 2-resonance ($\dot{\theta}_1 = \dot{\theta}_2 = 0$ in the integrable system (8), Fig. 5c).

In the first two cases above (cases 1 and 2) the parabolic 2-torus is a torus of closed invariant periodic orbits, and in the third case (case 3) it is a parabolic 2-torus of fixed points.

We examine numerically the effect of a small Hamiltonian perturbation on each of the above cases for system (8). The figures and descriptions below correspond to the following perturbation:

$$H_1 = \varepsilon_1 \left(1 - \frac{x^2}{2}\right) \cos(k_1\theta_1) + \varepsilon_2 \cos(k_2\theta_2), \quad \varepsilon = \varepsilon_1 = \varepsilon_2. \tag{21}$$

Other forms of Hamiltonian perturbations seems to produce similar results. Our form of visualization of the six-dimensional perturbed orbits in the figures presented here is by projections of the orbit on several sub-planes and sub-spaces of the six-dimensional phase space.

Considering our phenomenological model (Eqs. (7) and (8) with $\eta = 0$) with the perturbation (21), the model of a symmetric near-integrable 3 d.o.f. Hamiltonian exhibiting PRs is

$$H(x, y, \theta, I; \mu, \varepsilon) = \tfrac{1}{2}y^2 - I_1(\tfrac{1}{2}x^2) + \tfrac{1}{4}x^4 + \alpha_2 I_2 + (\tfrac{1}{2} + \alpha_1)\tfrac{1}{2}I_1^2 + \tfrac{1}{2}I_2^2 + \alpha_3 I_1 I_2$$
$$+ \varepsilon_1(1 - \tfrac{1}{2}x^2)\cos(k_1\theta_1) + \varepsilon_2 \cos(k_2\theta_2). \tag{22}$$

---

[11] In particular, in [26,27] it is proved that tangential 1-PR is generic and persistent for a class of smooth near-integrable 4 d.o.f. Hamiltonians.
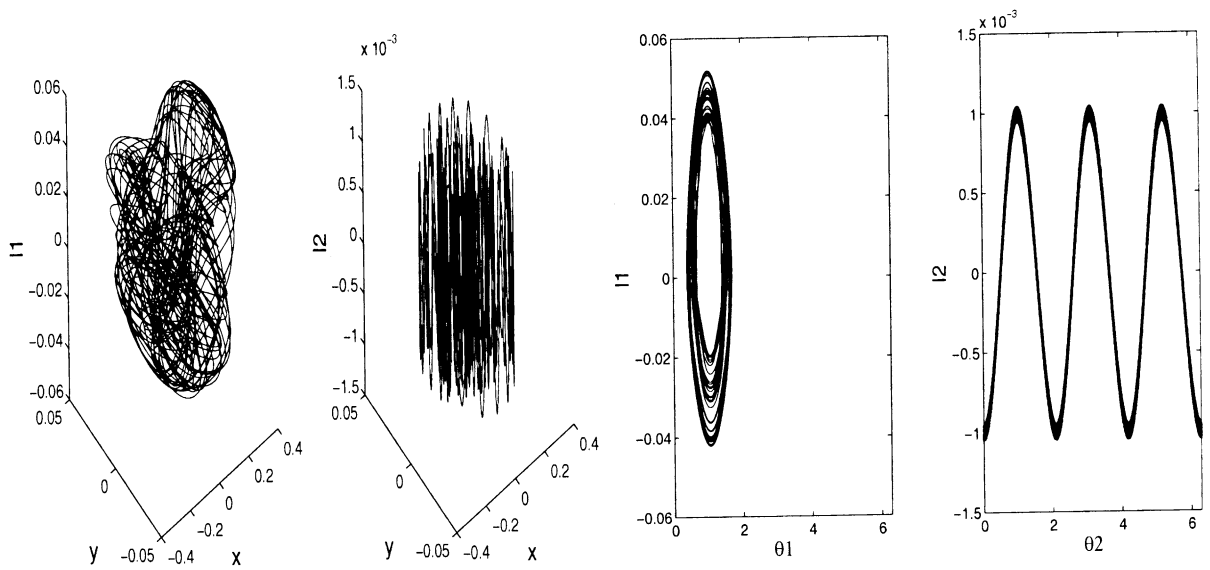
Fig. 10. A parabolic 1-resonance in I_1 direction. Initial conditions and parameters: $(x, y, \theta_1, I_1, \theta_2, I_2) = (0.2, 0, 1.57, 0, 1.57, 0)$, $\alpha_1 = 1$, $\alpha_2 = 1, \alpha_3 = 1, \varepsilon_1 = \varepsilon_2 = 1e - 3, H_0 \approx 4E - 4, t = 5000$. Notice the different scales of I_1 and I_2.
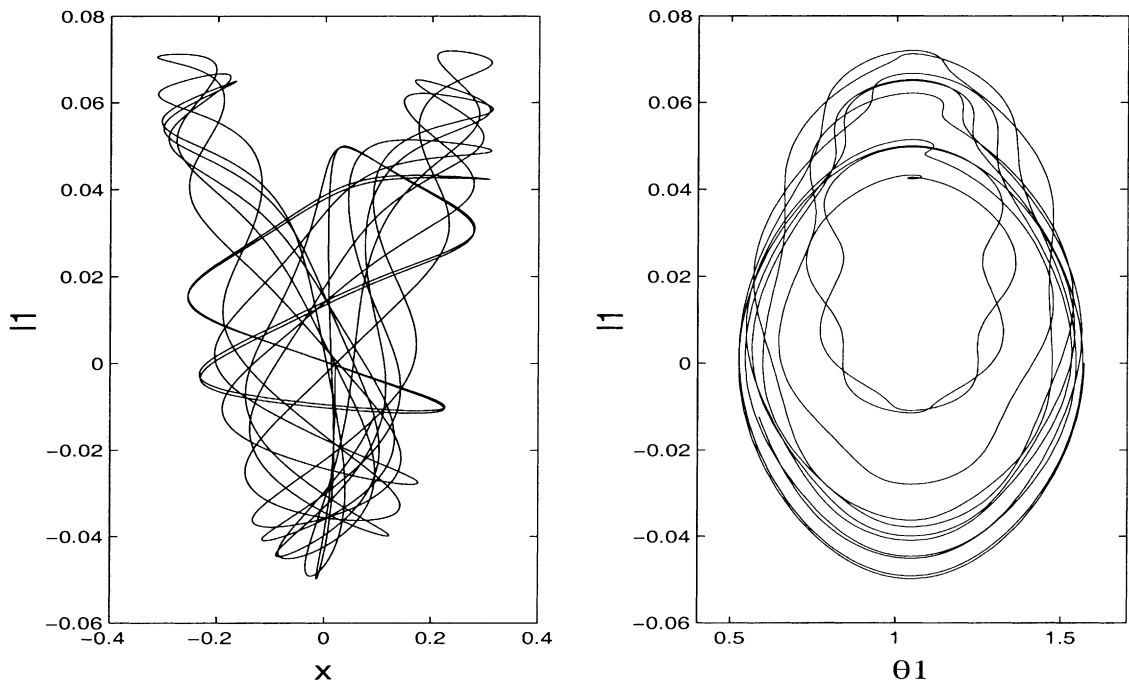
Fig. 11. A parabolic 1-resonance in I_1 direction. Initial conditions and parameters: $(x, y, \theta_1, I_1, \theta_2, I_2) = (0.2, 0, 1.57, 0, 1.57, 0)$, $\alpha_1 = 0.3, \alpha_2 = 1, \alpha_3 = 1, \varepsilon_1 = \varepsilon_2 = 1e - 3, H_0 \approx 4E - 4, t = 1000$.

2.2.1. Case 1: 1-PR in I_1 direction

The system corresponding to the Hamiltonian (22) exhibits 1-PR in I_1 direction for a set of initial conditions near the origin O_{xyI}, for *any* non-zero values of the parameters $\mu = (\alpha_1, \alpha_2, \alpha_3, k_1, k_2)$. Note that choosing any particular set of parameters corresponds to fixing a particular system—indeed, the existence of 1-PR is persistent, and this phenomenon occurs independently of external parameters on an open set of Hamiltonians (see Section 4 and [26,27] for further details).

The typical 1-PR in I_1 direction behavior is demonstrated by Figs. 10, 11 and 13 left. Fig. 10 presents the apparent chaotic behavior of the orbit, and the trapping in the PR zone in the (x, y, I_1) space (left plot) and in the (θ_1, I_1) plane (middle plot), together with the small oscillations of the orbit in the I_2 direction (right plot—the (θ_2, I_2) plane). Note the different scales for I_1 and I_2. Fig. 11 presents again a 1-PR in I_1 direction, with smaller α_1 value ($\alpha_1 = 0.3$). It demonstrates that the instabilities in I_1 are much stronger as α_1 is decreased. We propose that the source for this instability is the geometrical change of the unperturbed energy surface—for a given energy value near the PR, as α_1 is decreased the range of I_1 increases, approaching the unbounded range as $\alpha_1 \to 0$, where a flat PR occurs (see Section 2.1). We numerically observe that it becomes significant when $\alpha_1 < 0.5$. We stress that in all simulations of this case the perturbed orbit appears to reach the boundaries of its energy surface in I_1, which implies that the 1-PR in I_1 direction induces the strongest possible instabilities in I_1 (with respect to the boundaries of the energy surface), see Fig. 17 for illustration. The 1-PR in I_1 direction perturbed orbits exhibit a very similar structure to the 2 d.o.f. orbits of [34]. This may be explained by the fact that in this case (in the domain of interest—the vicinity of the origin O_{xyI}) the frequency $\omega_2 = \dot{\theta}_2$ is very large comparing to the other two frequencies (ω_0 and ω_1), hence the dependence on θ_2 may be averaged out (after rescaling), resulting in a 2 d.o.f. (averaged) system which exhibits the same qualitative behavior as the original (not averaged) 3 d.o.f. system. Note though that for 2 d.o.f. systems 1-PR is a co-dimension one phenomenon, and $n = 3$ is the *minimal* number of d.o.f. required for persistent appearance of 1-PR with no dependence on external parameters.

2.2.2. Case 2: 1-PR in I_2 direction

The Hamiltonian (22) exhibits 1-PR in I_2 direction for a set of initial conditions near $\{(x, y, I_1, I_2) = (0, 0, 0, I_2 = -\alpha_2)\}$, for *any* non-zero values of the parameters $\mu = (\alpha_1, \alpha_2, \alpha_3, k_1, k_2)$.

Typical behavior of 1-PR in I_2 direction orbits is presented in Figs. 12 and Fig. 13 right; Fig. 12 demonstrates that both actions exhibit quasi-periodic motion (see zoom in on the right plot); Fig. 13 presents a projection to the (x, y) plane of the orbits of cases 1 and 2 (left and right plots, respectively). While the 1-PR in I_1 direction orbit exhibits a PR chaos as in the 2 d.o.f. case, the 1-PR in I_2 direction orbit fills in a complicated structure. The structure which is seen in the right plot of Fig. 13 is composed of small sharp oscillations of the orbit in the (x, y) plane; these oscillations may be seen in the second plot from the left in Fig. 12, where the orbit is presented for a very short time scale ($t = 300$ in this figure); as these oscillations are very dense, they are hard to detect on plots of large time scale orbits ($t = 8700$ in the corresponding orbit projection on the (x, y) plane in Fig. 13), nevertheless a large time scale is required to see the complicated structure created in the (x, y) plane; in fact, the time interval of Fig. 13 is required for one completion of the seen shape, and the structure repeats itself over and over again (each time a bit smaller) when the orbit is integrated for a longer time then presented. Such complicated structures are observed for a range of initial conditions and parameters near 1-PR in I_2 direction.

The different roles of the actions in the system is now apparent; substantially different behavior is observed when the resonance direction coincides with the direction of the bifurcating action (I_1) than otherwise. As this separation of roles of the actions is achieved by a symplectic change of variables on the integrable Hamiltonian, the two scenarios are expected to appear in any general near-integrable Hamiltonian exhibiting PRs.
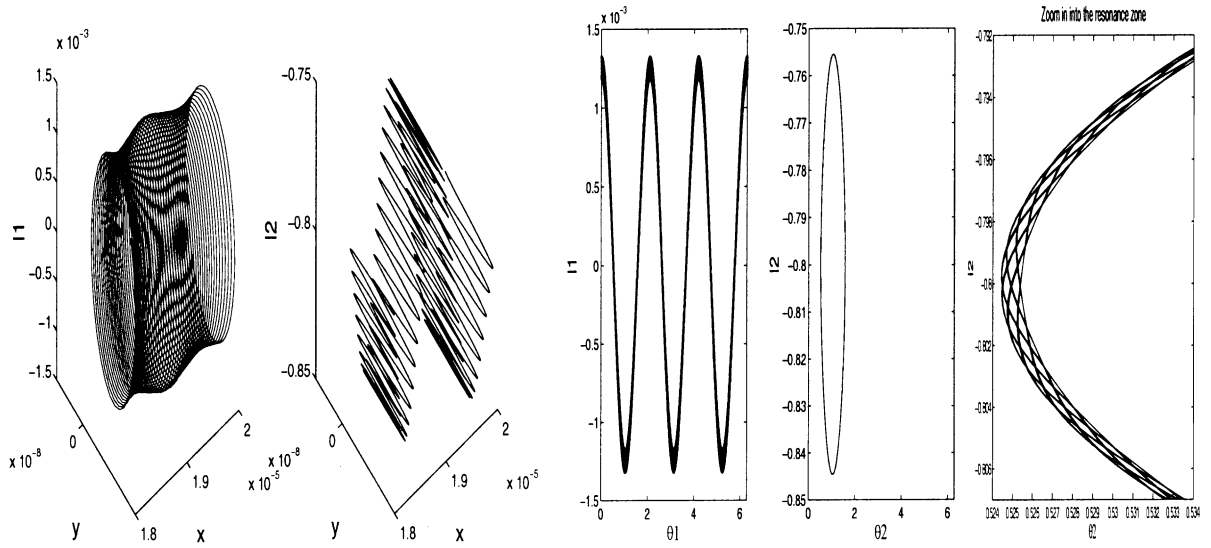
Fig. 12. A parabolic 1-resonance in I_2 direction. Initial conditions and parameters: $(x, y, \theta_1, I_1, \theta_2, I_2) = (2E - 5, 0, 1.57, 0, 1.57, -0.8)$, $\alpha_1 = 1, \alpha_2 = 0.8, \alpha_3 = 1, \varepsilon_1 = \varepsilon_2 = 1e - 3, H_0 \approx 4E - 4$. Left two plots: $t = 300$, right plots: $t = 5000$. Notice the different scales of I_1 and I_2.

2.2.3. Case 3: 2-PR

2-PR is a co-dimension one phenomenon for 3 d.o.f. Hamiltonians. The extra parameter required for appearance of 2-PR in Hamiltonian (22) is α_2. Setting $\alpha_2 = 0$, (22) exhibits 2-PR for a set of initial conditions near the origin, O_{xyI}, for any non-zero values of the remaining parameters: $\alpha_1, \alpha_3, k_1, k_2$. Hence, the model Hamiltonian for this
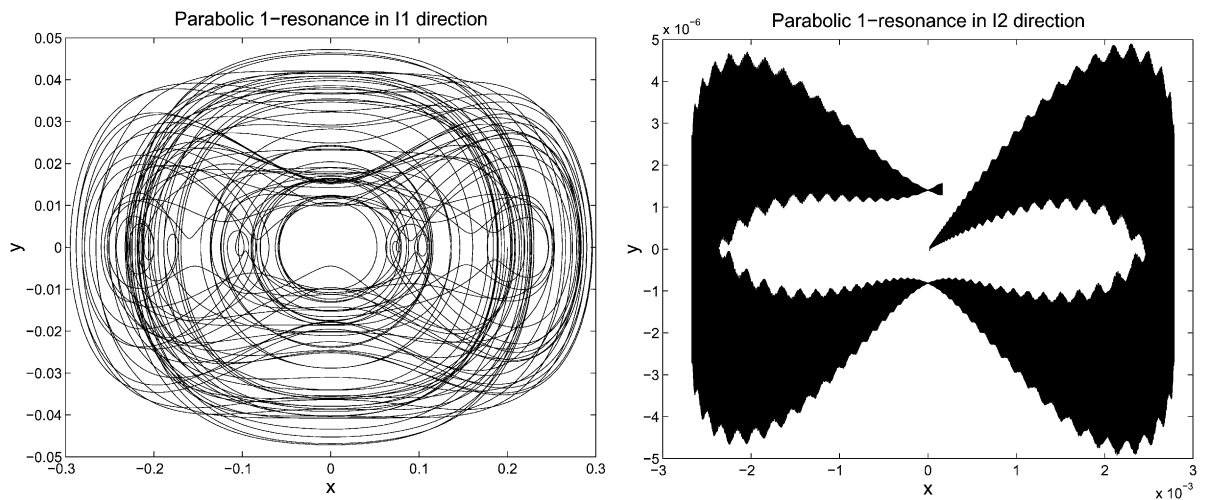
Fig. 13. Parabolic 1-resonances projected on the (x, y) plane. Initial condition and parameters: as in Fig. 10 with $t = 5000$ and Fig. 12 with $t = 8700$, respectively.
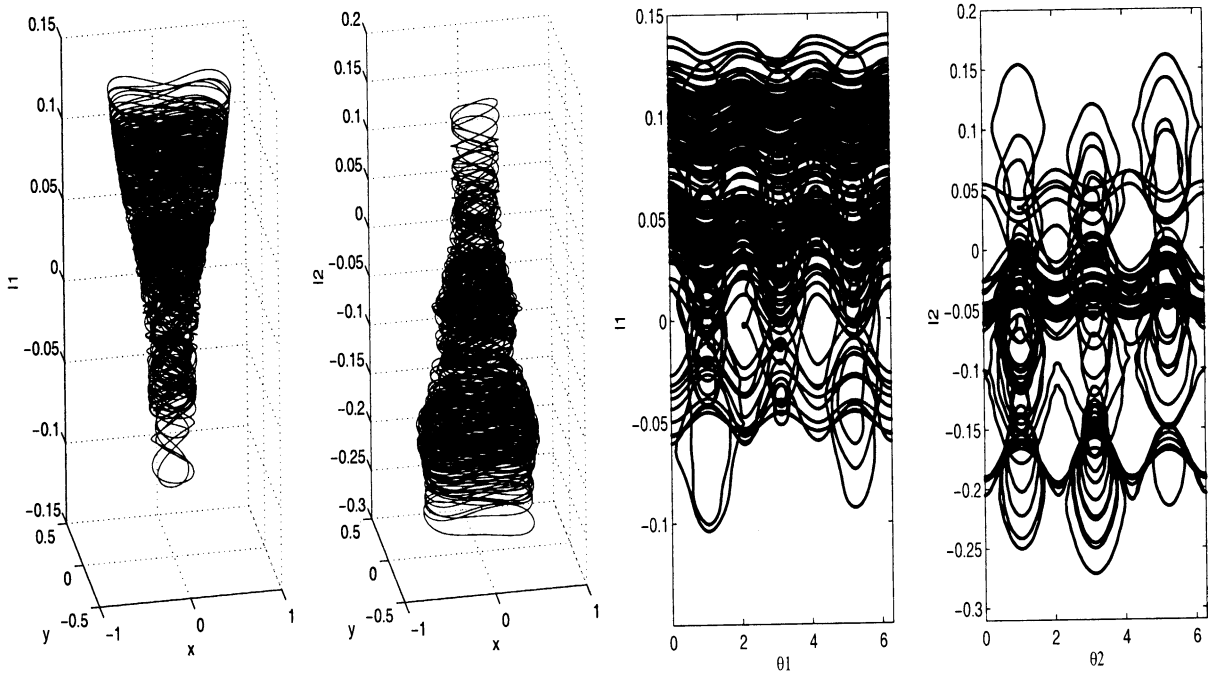
Fig. 14. A parabolic 2-resonance. Initial conditions and parameters: $(x, y, \theta_1, I_1, \theta_2, I_2) = (0.2, 0, 1.57, 0, 1.57, 0)$, $\alpha_1 = 1.1$, $\alpha_2 = 0$, $\alpha_3 = 2$, $\varepsilon_1 = \varepsilon_2 = 1e - 3$, $H_0 \approx 4E - 4$, $t = 5000$.

case may be written in the form

$$H(x, y, \theta, I; \mu, \varepsilon) = \tfrac{1}{2}y^2 - I_1(\tfrac{1}{2}x^2) + \tfrac{1}{4}x^4 + (\tfrac{1}{2} + \alpha_1)(\tfrac{1}{2}I_1^2) + \tfrac{1}{2}I_2^2 + \alpha_3 I_1 I_2$$
$$+ \varepsilon_1(1 - \tfrac{1}{2}x^2)\cos(k_1\theta_1) + \varepsilon_2 \cos(k_2\theta_2). \tag{23}$$

Typical behavior of 2-PR orbits is presented in Fig. 14. Fig. 14 demonstrates that the resonance zones and large instabilities are created in both actions. Notice that the *system is non-degenerate*. This behavior should be contrasted with the 2 d.o.f. case, in which large instabilities in the action variable are possible only in degenerate cases, when the necessary conditions for KAM theory fail.

We prove in [26,27] that cases 1 and 2 (1-PR) are persistent in 3 d.o.f. near-integrable Hamiltonian systems without the use of external parameters (where the actions serve as internal parameters), and that case 3 (2-PR) is persistent in a one parameter family of near-integrable 3 d.o.f. Hamiltonian systems. Moreover, it is proved in [26,27] that 2-PR is persistent in 4 (or more) d.o.f. near-integrable Hamiltonian systems without the use of external parameters; numerical experiments suggest that the behavior near 2-PR in higher-dimensional systems ($n \geq 4$) is similar to the one presented here (Fig. 14).

2.2.4. Degenerate (flat) PRs

Flat PRs correspond to co-existence of a 1-PR or a 2-PR with a specific additional degeneracy in the unperturbed system. This specific degeneracy is a co-existence of a whole family of resonant tori of different stability types on a certain unperturbed energy surface.

The single case of flat PR which was presented for 2 d.o.f. systems in [34,36] has several generalizations in the 3 d.o.f. setting: one type of flat 1-PR, and two types of flat 2-PR.

One set of generalizations is simply attained by setting $\alpha_1 = 0$ in the Hamiltonian (22) (see Section 2.1). As 1-PR is attained without dependence on external parameters, the model near-integrable 3 d.o.f. Hamiltonian attaining flat 1-PR is

$$H(x, y, \theta, I; \mu, \varepsilon) = \tfrac{1}{2}y^2 - I_1(\tfrac{1}{2}x^2) + \tfrac{1}{4}x^4 + \alpha_2 I_2 + \tfrac{1}{4}I_1^2 + \tfrac{1}{2}I_2^2 + \alpha_3 I_1 I_2$$
$$+ \varepsilon_1(1 - \tfrac{1}{2}x^2)\cos(k_1\theta_1) + \varepsilon_2\cos(k_2\theta_2), \tag{24}$$

where flat 1-PR is exhibited by (24) for a set of initial conditions near the origin, O_{xyI}, for any non-zero values of the remaining parameters $(\alpha_2, \alpha_3, k_1, k_2)$. This type of flat 1-PR corresponds to appearance of a whole family of 1-resonant elliptic 2-tori on the same unperturbed energy surface, emanating from a 1-resonant parabolic 2-torus. A flat 1-PR orbit of the perturbed system with Hamiltonian (24) may be seen in Fig. 16. As 2-PR is attained by setting $\alpha_2 = 0$ in the Hamiltonian (22) (resulting in Hamiltonian (23)), setting in addition $\alpha_1 = 0$, the model near-integrable 3 d.o.f. Hamiltonian attaining this type of flat 2-PR is

$$H(x, y, \theta, I; \mu, \varepsilon) = \tfrac{1}{2}y^2 - I_1(\tfrac{1}{2}x^2) + \tfrac{1}{4}x^4 + \tfrac{1}{4}I_1^2 + \tfrac{1}{2}I_2^2 + \alpha_3 I_1 I_2 + \varepsilon_1(1 - \tfrac{1}{2}x^2)\cos(k_1\theta_1)$$
$$+ \varepsilon_2\cos(k_2\theta_2), \tag{25}$$

where again, the perturbed system corresponding to (25) exhibits flat 2-PR for a set of initial conditions near the origin, O_{xyI}, for any non-zero values of the remaining parameters (α_3, k_1, k_2). The type of flat 2-PR exhibited by (25), corresponds to appearance of a whole family of 1-resonant elliptic 2-tori on the same unperturbed energy surface, emanating from a 2-*resonant parabolic 2-torus* (a parabolic torus of fixed points). An orbit starting near such a flat 2-PR is presented in Fig. 18.

Another generalization is attained by setting $\alpha_2 = 0$ and $\alpha_1 = \alpha_3^2 \neq 0$ in the Hamiltonian (22) (see end of Section 2.1). The resulting flat 2-PR corresponds to a whole family of elliptic 2-resonant tori, emanating from a 2-resonant parabolic torus (tori of fixed points), all residing on the same unperturbed energy surface. The simplest model attaining this type of flat 2-PR is

$$H(x, y, \theta, I; \mu, \varepsilon) = \tfrac{1}{2}y^2 - I_1(\tfrac{1}{2}x^2) + \tfrac{1}{4}x^4 + (\tfrac{1}{2} + \alpha_3^2)\tfrac{1}{2}I_1^2 + \tfrac{1}{2}I_2^2 + \alpha_3 I_1 I_2$$
$$+ \varepsilon_1(1 - \tfrac{1}{2}x^2)\cos(k_1\theta_1) + \varepsilon_2\cos(k_2\theta_2), \tag{26}$$

where this flat 2-PR is exhibited by (26) for a set of initial conditions near the origin, O_{xyI}, for any non-zero values of the remaining parameters (α_3, k_1, k_2). A flat 2-PR orbit of the Hamiltonian (26), exhibiting order one instabilities in both actions along the direction $I_2 = -\alpha_3 I_1$ may be seen in Figs. 19 and 20.

Next we describe in more details these three cases of flat and near-flat [12] PRs exhibited by Hamiltonian (22), and compare them with the 2 d.o.f. flat PR, with the use of Figs. 15–20.

The numerical simulations of "case 1" (1-PR in I_1 direction) with $\alpha_1 < 0.5$ demonstrated that the behavior in the near-flat case is qualitative similar to the one observed for 2 d.o.f. models (see [34,36] and Fig. 15, in which $\alpha_2 = \alpha_3 = \varepsilon_2 = 0$—making (22) a 2 d.o.f. Hamiltonian). In both cases (see Figs. 15 and 16) the orbit perform far flights in the positive direction of I_1 along the successive connected elliptic resonance zones, and returns repeatedly to the PR zone (near the origin O_{xyI_1}). However, perhaps due to the small oscillations in the I_2 direction, it appears that the order one instabilities in I_1 direction develop *slower* in the 3 d.o.f. case. The small oscillations in the I_2 direction, performed by the flat 1-PR orbit, may be seen in the right plots of Fig. 16: in

---

[12] Recall, here the flat PR has $\alpha_1 = 0$, whereas near-flat PR has $\alpha_1 \ll 1$ (and in practice $\alpha_1 < 0.5$).
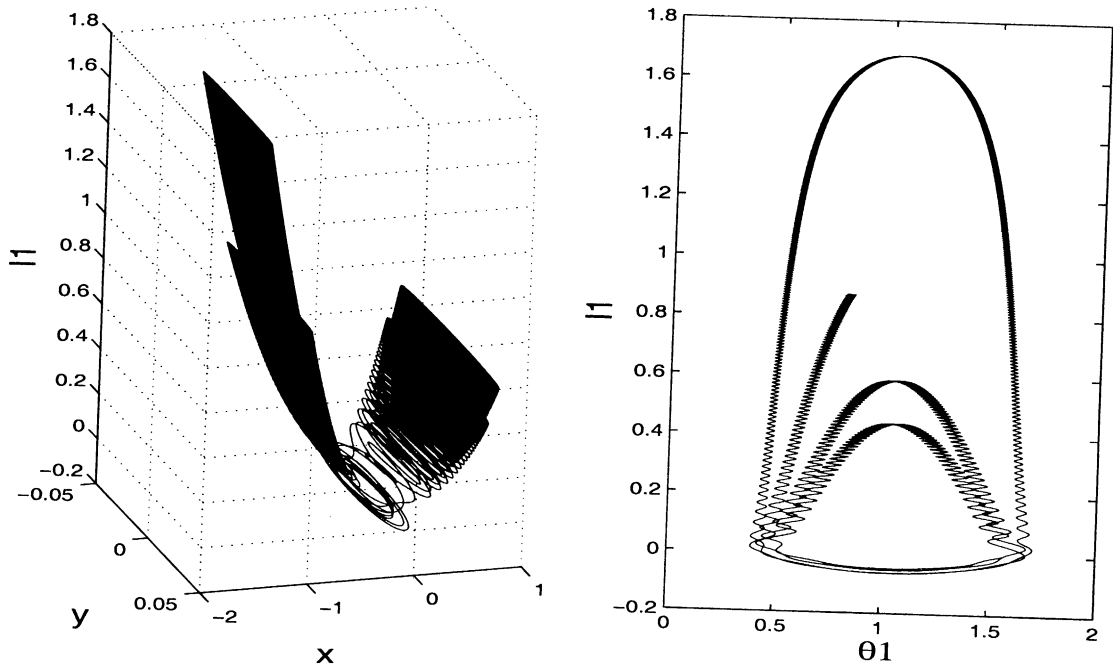
Fig. 15. A flat PR in a 2 d.o.f. system. Initial conditions and parameters: $(x, y, \theta_1, I_1, \theta_2, I_2) = (0.2, 0, 1.57, 0, 1.57, 0), \alpha_1 = 0, \alpha_2 = 0, \alpha_3 = 0,$ $\varepsilon_1 = 1e - 3, \varepsilon_2 = 0, H_0 \approx 4E - 4, t = 5000.$
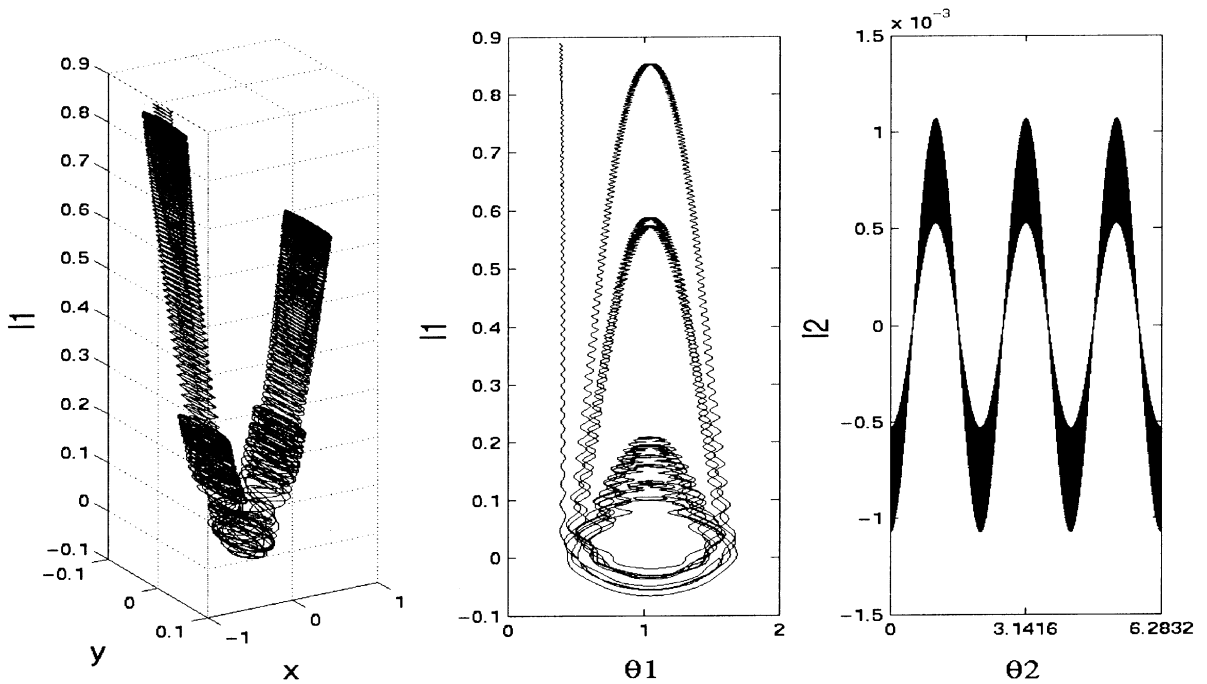
Fig. 16. A flat parabolic 1-resonance in a 3 d.o.f. system. Initial conditions and parameters: $(x, y, \theta_1, I_1, \theta_2, I_2) = (0.2, 0, 1.57, 0, 1.57, 0),$ $\alpha_1 = 0, \alpha_2 = 1, \alpha_3 = 1, \varepsilon_1 = \varepsilon_2 = 1e - 3, H_0 \approx 4E - 4, t = 5000.$
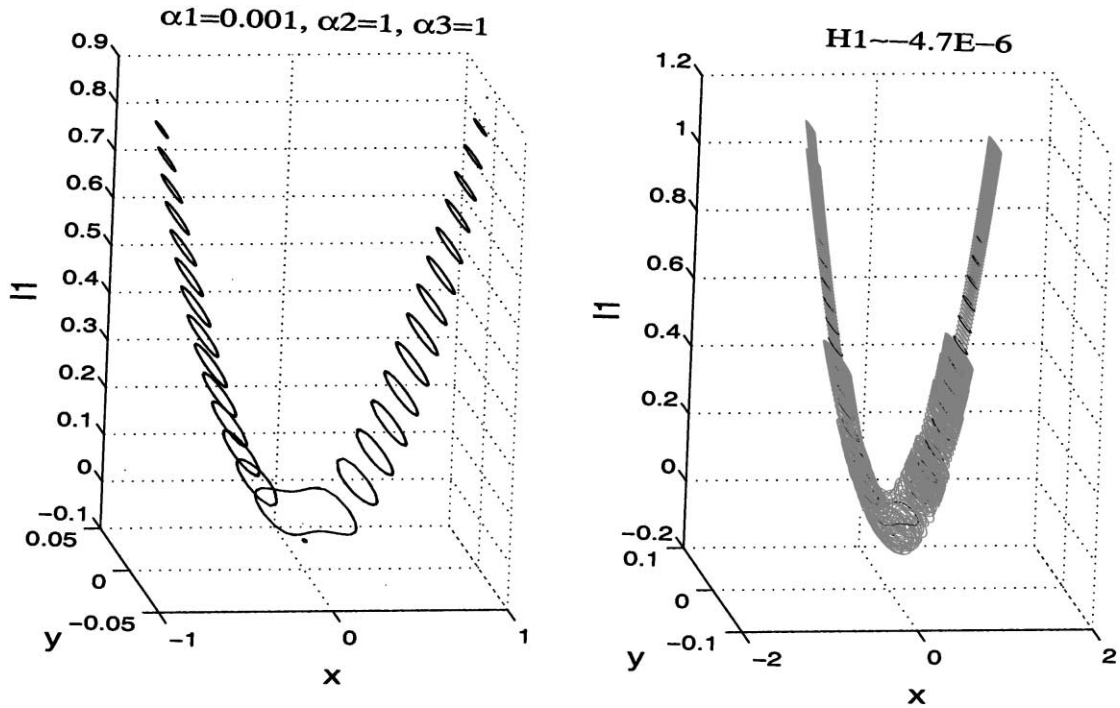
Fig. 17. A near-flat parabolic 1-resonance in a 3 d.o.f. system, and the corresponding unperturbed energy surface. Initial conditions and parameters: $(x, y, \theta_1, I_1, \theta_2, I_2) = (0.2, 0, 1.57, 0, 1.57, 0)$, $\alpha_1 = 0.001$, $\alpha_2 = 1$, $\alpha_3 = 1$, $\varepsilon_1 = \varepsilon_2 = 1e - 3$, $H_0 \approx 4E - 4$, $t = 8000$.

the upper right plot the orbit is plotted in the (θ_2, I_2) plane for a long run time ($t = 5000$), hence the repeated small oscillations appear as a "black region"; for the convenience of the viewer we present in the lower right plot in Fig. 16 a small segment of this orbit ($t = 500$), in which the oscillations in the I_2 direction may be more clearly seen—the "black region" in the right upper plot consists of such oscillations. Fig. 17 demonstrates that near-flat 1-PR orbits cover the corresponding I_2 slices of the unperturbed energy surface. Furthermore, the orbits repeatedly pass through the PR zone and repeatedly reach the boundaries (in I_1) of these energy slices. In the right plot of this figure we present the orbit (in gray) covering the corresponding unperturbed energy surface (in black), which is presented separately on the left plot; the unperturbed energy surface in this figure corresponds to the fixed value of $I_2 = 0$, and it is presented by the sequence of (x, y) orbits calculated for a sequence of I_1 values in the interval between the elliptic equilibria bounding this energy surface from below and above in I_1 (see Section 2.1).

The two other cases of flat 2-PR have perturbed orbits which wander through successive resonance zones which are created in both actions directions, see Figs. 18–20. In the first case (Fig. 18; $\alpha_1 = \alpha_2 = 0$, which brings the Hamiltonian (22) to the form (25)), a parabolic resonant torus of fixed points and a family of elliptic tori of *periodic orbits* reside on the same unperturbed energy surface, whereas in the second case a parabolic resonant torus of fixed points and a family of elliptic tori of *fixed points* reside on the same unperturbed energy surface (Figs. 19 and 20; $\alpha_2 = 0$, and $\alpha_1 = \alpha_3^2$, which brings the Hamiltonian (22) to the form (26)). Fig. 18 demonstrates that the structure of the flat 2-PR orbits corresponding to the Hamiltonian (25) combines (as may be expected from the construction) the behavior observed for the case of 2-PR near the
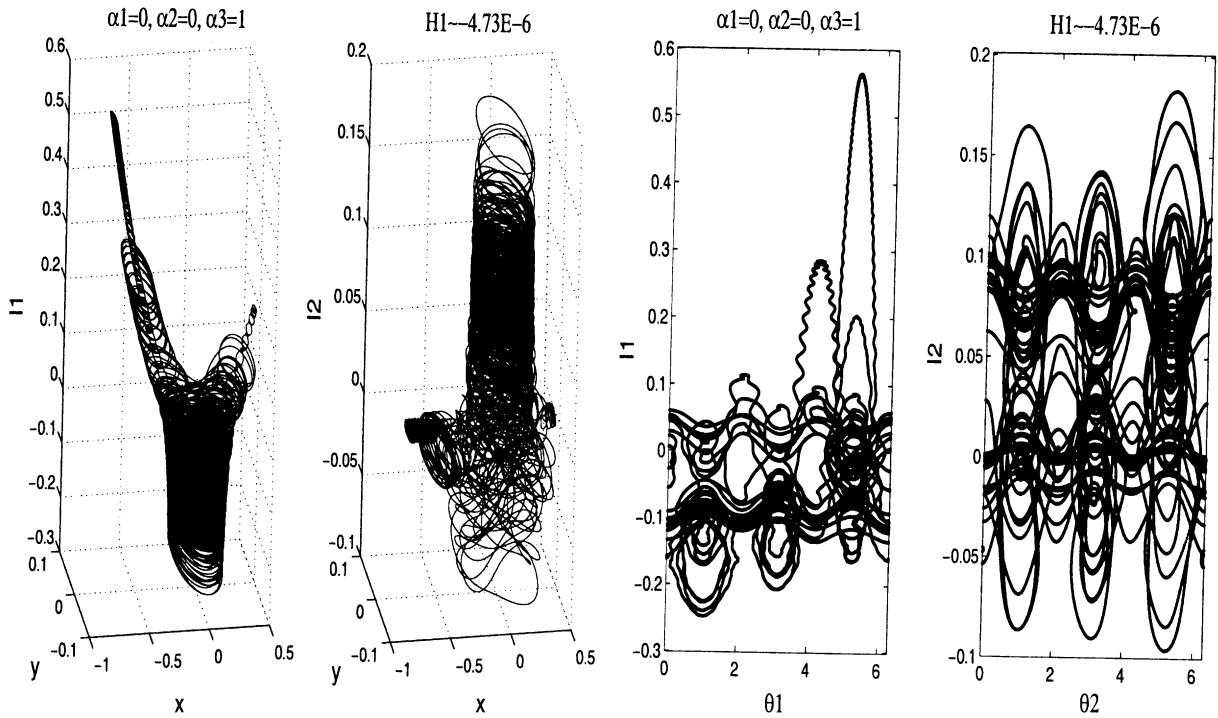
Fig. 18. A flat parabolic 2-resonance. Initial conditions and parameters: $(x, y, \theta_1, I_1, \theta_2, I_2) = (0.2, 0, 1.57, 0, 1.57, 0), \alpha_1 = 0, \alpha_2 = 0, \alpha_3 = 1$, $\varepsilon_1 = \varepsilon_2 = 1e - 3$, $H_0 \approx 4E - 4$, $t = 8000$.

PR zone (see Fig. 14) and for the case of flat 1-PR in the flights of the orbit along the elliptic resonant family (see Fig. 16).

In Fig. 19 (Hamiltonian (26)), the order one instabilities in all phase space directions exhibited by the flat 2-PR orbit in the (x, y, I_1) and (x, y, I_2) spaces are shown in the top plots, and the corresponding slices of the unperturbed energy surfaces are shown in the bottom plots. It is seen that although these slices of the unperturbed energy surfaces are small the instabilities are large. Indeed, since the instabilities occur in both actions, slices attained by fixing one of them do not reflect the unboundedness of the energy surface in the $I_1 = -I_2$ direction, the direction along which the instabilities develop (see Fig. 9). Fig. 20 presents the projection of the same perturbed orbit on the (θ_1, I_1) and (θ_2, I_2) planes. In this figure the spring like structure of the orbit which passes through the multi-resonance zones is shown.

The most important feature of the instabilities associated with the flat, near-flat and tangential PRs is that they develop on relatively short time scales. For example, in the 2-PR case large instabilities occur, but their development is relatively slow, obeying one time scale, while in the cases of the flat PRs, two time scales (slow and fast) coexist. On the slow time scale, the orbit is trapped in a resonance zone, and on the fast time scale it makes far trips sliding through successive resonance zones. In the tangential 2-resonance case (a persistent co-dimension 2 phenomenon for 3 d.o.f. Hamiltonians [26,27]) these fast trips may occur in all phase space directions simultaneously. Note that 2-PR and flat (near-flat, tangential) 2-PRs are a higher-dimensional apparatus, and the *minimal* number of d.o.f. in the Hamiltonian needed for their occurrence is $n = 3$ (see [26,27] for the description of the higher-dimensional cases and proofs).
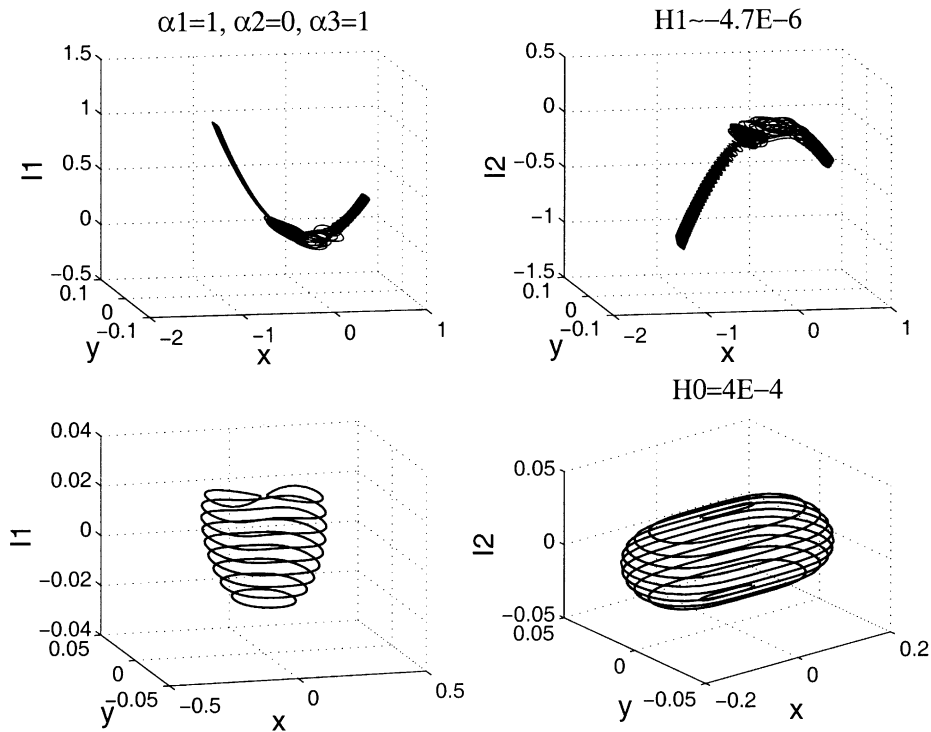
Fig. 19. A flat parabolic 2-resonance. An orbit and the corresponding unperturbed energy surface are projected on the (x, y, I_1) and (x, y, I_2) spaces. Initial conditions and parameters: $(x, y, \theta_1, I_1, \theta_2, I_2) = (0.2, 0, 1.57, 0, 1.57, 0)$, $\alpha_1 = 1, \alpha_2 = 0, \alpha_3 = 1$, $\varepsilon_1 = \varepsilon_2 = 1e - 3$, $H_0 \approx 4E - 4, t = 8000$.

It still remains to calculate analytically the rate of instability created in each of the cases of parabolic and tangential PR; this work is under process.

3. The motion of weather balloons—a model

Here we present a 3 d.o.f. model (the Hamiltonian (27)), describing the motion of particles (weather balloons) on a rotating sphere (geopotential surfaces of the earth atmosphere) which are subject to a conservative force (traveling wave pressure term), which breaks the angular symmetry. A third d.o.f. is added to the 2 d.o.f. atmospheric model studied in [35,36]; this additional d.o.f. describes the small altitude oscillations of the weather balloons.

For the 2 d.o.f. case (taking $\varepsilon_2 = 0$, $D_2 = 0$ in (27)) the global phase space structure of the unperturbed system has been described in [35] by the shaded energy–momentum bifurcation diagrams. In [34,36] the phenomena of PR was discovered, and has been shown to exist in this model; it has been numerically demonstrated that near-flat PR is a source of strong, yet rare phase space instability, with qualitative agreement to the observations of motion of weather balloons in field experiments.

To describe the weather balloon motion on a rotating sphere with a given traveling pressure wave velocity c, we use normalized, relative spherical coordinate system; let ϕ be the latitude on the sphere and v its conjugate northward velocity, Λ_1 the longitude in the traveling wave frame and D_1 its conjugate angular momentum. Finally, let Λ_2
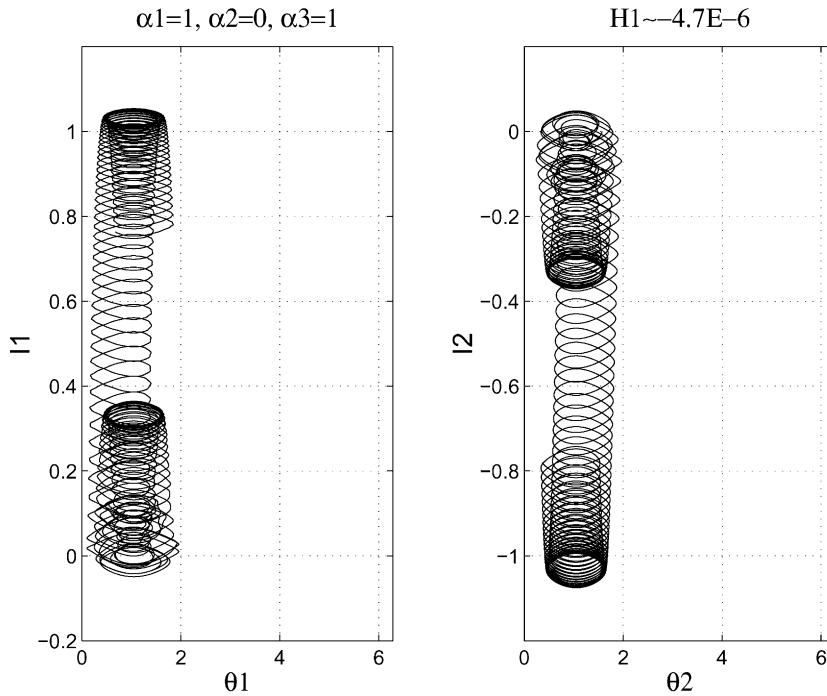
Fig. 20. A flat parabolic 2-resonance. Projections of the orbit on the (θ_1, I_1) and (θ_2, I_2) planes. Initial conditions and parameters as in Fig. 19.

denote the normalized vertical oscillation amplitude and D_2 its conjugate momenta. The new 3 d.o.f. Hamiltonian is given by

$$
\begin{aligned}
H(\phi, v, \Lambda, D; \mu, k, \varepsilon) &= \frac{v^2}{2} + \frac{1}{8}\left(\frac{2D_1}{\cos(\phi)} - \cos(\phi)\right)^2 + \frac{D_2^2}{2} - cD_1 + aD_2\left(D_1 - \frac{1}{2}\right) \\
&\quad + bD_2 + B(\phi; \beta) + A(\phi)(\varepsilon_1 \sin(k_1 \Lambda_1) + \varepsilon_2 \sin(k_2 \Lambda_2)) \\
&= H_0(\phi, v, D; \mu) + H_1(\phi, v, \Lambda, D; \mu, k, \varepsilon), \\
(\phi, v, \Lambda, D) &\in U \subseteq \mathbb{R}^2 \times \mathbb{T}^2 \times \mathbb{R}^2, \quad k \in \mathbb{Z}, \beta, \varepsilon \in \mathbb{R}^2, \quad |\varepsilon| \ll 1,
\end{aligned}
\tag{27}
$$

where $\mu = (a, b, c, k_1, k_2, \beta)$ with $a, b, c, \beta \in \mathbb{R}$, $k_1, k_2 \in \mathbb{Z}$, $\varepsilon_1, \varepsilon_2 \ll 1$. $A(\phi)$ and $B(\phi)$ represent the latitude-dependent amplitudes of the traveling pressure wave and the constant pressure term, respectively. In our numerical simulations they are taken to be of the form:

$$
A(\phi) = \cos(\phi), \qquad B(\phi; \beta) = \beta \tanh\left(\frac{\phi^2 - \phi_0^2}{\alpha}\right), \quad \phi_0 = 30° \approx 0.5236, \quad \alpha = 0.05, \quad \beta = -0.001.
\tag{28}
$$

Namely, $A(\phi)$ is simply the first symmetric harmonic and $B(\phi)$ represents a steady pressure term that is monotonically decreasing pole-ward, allowing strong zonal jets to appear near ϕ_0. The numerical values appearing in (28) correspond to rough estimates of physical relevant parameter values.

In the 2 d.o.f. case (the Hamiltonian (27), with $\varepsilon_2 = 0$, $D_2 = 0$) a PR occurs for $D_1 = 0.5$, $c = 0$, and a flat (degenerate) PR if in addition $B(\phi) = 0$ (the physical relevant case is $|B(\phi)| \ll 1$, hence it corresponds to
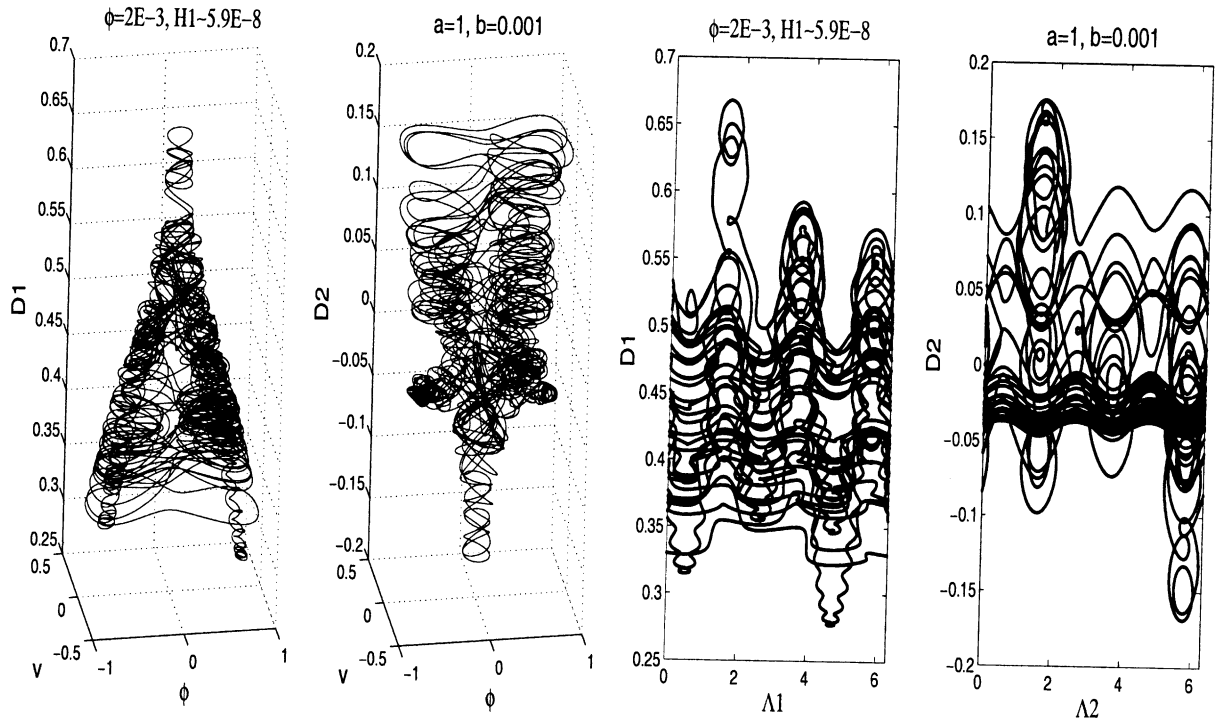
Fig. 21. A near-flat parabolic 2-resonance in the 3 d.o.f. atmospherical model. Initial conditions and parameters: $(\phi, v, \Lambda_1, D_1, \Lambda_2, D_2) = (2E - 3, 0, 1E - 5, 0.5, 1E - 5, 0), a = 1, b = 0.001, \varepsilon_1 = \varepsilon_2 = 1e - 3, \beta = -0.001, t = 5000$.

a nearly flat PR). These PRs correspond to two simultaneous phenomena—the change in the linear stability in latitude direction of particles motion about the equator (about $(\phi, v) = (0, 0)$) and the coincidence of the traveling wave speed with the west-ward speed along the equator $(\dot{\Lambda}_1|_{(\phi, v, D_1) = (0, 0, 0.5)} \equiv 0)$. Adding a third d.o.f. to this model allows PR to occur without any external parameters. In (27), the second constant of motion, D_2, replaces the mathematical role of the parameter c of the 2 d.o.f. model in [35]. Hence, for any value of c there exist a D_2 value for which a 1-PR occurs for some $D(c)$ $(D(c = 0) = (D_{1_{\text{PR}}}, D_{2_{\text{PR}}}) = (0.5, 0))$.

Here, the model (27) serves us as a test case application for our findings for the phenomenological model. Indeed, all types of behavior which are described above for PRs and flat/near-flat PRs that are observed for the phenomenological model (8) are observed for this atmospheric model as well. For example, see Fig. 21, where an orbit, exhibiting a near-flat 2-PR, projected on the sub-spaces (ϕ, v, D_1), (ϕ, v, D_2) and sub-planes (Λ_1, D_1), (Λ_2, D_2) are shown (the plots are ordered from left and right plots, respectively). Compare this figure with Fig. 18 of the phenomenological model. This near-flat 2-PR, which results in instabilities in all phase space directions simultaneously, is a 3 d.o.f. phenomenon.

4. Persistence of PRs

We have demonstrated that a simple phenomenological model is rich enough to attain PRs of various kinds. The possibility to construct such a model in a straight forward way follows from the *persistence* of PRs in 3 d.o.f. systems. In [26,27], we prove several theorems regarding the persistence of PRs with various properties in near-integrable n

d.o.f. Hamiltonian systems ($n \geq 3$). The implications of these theorems on the persistence of resonant 2-tori in 3 d.o.f. near-integrable systems are listed below:

Theorem 1. *The existence of a normally parabolic* 1*-resonant torus is persistent for smooth near-integrable* 3 *d.o.f. Hamiltonian systems, without the use of external parameters. Each such torus consists of a* 1*-dimensional family of circles.*

Corollary 2. *The occurrence of a parabolic* 1*-resonance is persistent in the space of smooth near-integrable* 3 *d.o.f. Hamiltonian systems.*

Theorem 3. *The existence of a normally parabolic* 2*-resonant torus (i.e. a normally parabolic* 2*-torus of fixed points) is persistent in a one parameter family of smooth integrable* 3 *d.o.f. Hamiltonian systems.*

Corollary 4. *The occurrence of a parabolic* 2*-resonance is persistent in a one parameter family of smooth near-integrable* 3 *d.o.f. Hamiltonian systems.*

Notice that the first corollary deals with cases 1 and 2 of Section 2.2 and the second corollary deals with case 3. Indeed, for cases 1 and 2 we do not need to fix any parameters in our model (8), whereas case 3 requires fixing one parameter ($\alpha_2 = 0$).

Since our Hamiltonian (7) depends on the actions only up to quadratic terms, we need to fix only one additional parameter to obtain flat PRs. More generally, fixing one additional parameter results in a tangential PR, which exhibits similar instabilities to the ones obtained in the flat case (see [26,27] for more details):

Theorem 5. *The existence of an infinitesimal family of normally elliptic and/or normally hyperbolic resonant tori together with a normally parabolic* 1*-resonant (respectively* 2*-resonant) torus, on the same energy surface, is persistent in a one parameter (respectively two parameter) family of smooth integrable* 3 *d.o.f. Hamiltonian systems.*

Corollary 6. *The occurrence of a tangential parabolic* 1*-resonance (respectively* 2*-resonance) is persistent in a one parameter (respectively two parameter) family of smooth near-integrable* 3 *d.o.f. Hamiltonian systems.*

5. Summary and conclusions

By investigating a near-integrable Hamiltonian with an integrable part, which is constructed by polynomial expansion in normal coordinates, we demonstrated that the phenomena of PR appears in a persistent way in 3 d.o.f. near-integrable systems (this follows from the persistence theorems which are proved in [26,27]). PRs typically appear in systems in which the integrable part is non-separable. We found that *different types of PR correspond to different dynamical phenomena*. There are two *different* persistent 1-PR scenarios for 3 d.o.f. systems (both appearing without dependence of the system on external parameters); in one case the action governing the stability of the 2-tori is also involved in the resonance, whereas in the second case one action governs the stability of the 2-tori and the other action is involved in the resonance. The first case is a direct generalization of the PR appearing in 2 d.o.f. systems, whereas the second corresponds to a cross product of a parabolic bifurcation and a resonance. Numerical simulations suggest that the former gives relatively strong instabilities, which occur on a fast time scale. More precisely, the non-bifurcating action oscillates slightly while the action responsible for the PR varies as far as possible—it covers the full range of the unperturbed allowed region of motion (with a nearly fixed second action). The simulations demonstrated that the instabilities near the degenerate flat PR ($\alpha_1 = 0$ in Eq. (22)) leave their mark

even on relatively large non-degeneracy parameter ($\alpha_1 < 0.5$). It was proposed that in this case *the geometry of the unperturbed energy surfaces determines the extent of the instability*—the smaller the non-degeneracy parameter is, the larger the range of the bifurcation action in the nearby energy surfaces and hence the larger is the instability. The other kind of 1-PR (in the direction of the non-bifurcating action) does not exhibit strong instabilities, yet produces interesting structures; the actions vary quasi-periodically (the resonant action on a larger scale), and the motion in the normal plane fills a complicated structure.

A normally parabolic 2-torus of fixed points (the corresponding behavior of nearby perturbed orbits is called a 2-PR) appears in a persistent way in a one parameter family of 3 d.o.f. systems. We demonstrated that in this case large (yet slow in comparison to the flat cases) instabilities appear even in the non-degenerate case. We have seen that further degeneracies of this case, corresponding to flat 2-PRs result in fast and large (order 1) instabilities in all phase space directions. 2-PRs are a higher-dimensional phenomena, and $n = 3$ is the *minimal* number of d.o.f. required for their appearance; $n = 4$ is the minimal number of d.o.f. required for persistent appearance of the non-degenerate 2-PR, without dependence on external parameters; see [26,27] for more details on the higher-dimensional cases.

The main analytical tool we have used to analyze the system is the construction of bifurcation diagrams in the space of constants of motion. We showed that they give a global and full description of the behavior of the integrable system. Moreover, these bifurcation diagrams are used to deduce which scenarios are expected in the corresponding near-integrable system. For example, we saw that the first kind of 1-PR (in the direction of the bifurcating action) corresponds to a change of stability at a fold of the bounding surface of the allowed region of motion, and a flat 1-PR corresponds to resonance lines which include the parabolic point and which are perpendicular to the energy axis (hence correspond to *unbounded* energy surfaces).

The main idea conveyed here is that PRs are a source of instability which appear inevitably in a large class of higher-dimensional systems. Here we have constructed a simple model to demonstrate how strong the influence of such instabilities may become (see also [28]), and in a later work [26,27] we examine how the mechanisms of insta-bilities can become more and more degenerate (hence more influential) as the dimensionality of the system grows.

Many issues remain to be addressed in the future. First, a precise estimate (numerical and analytical) of the instability strength needs to be established and compared to other mechanisms of instabilities in 3 d.o.f. systems. Since the motion appears to be recurrent (with long excursions), this requires a good definition of escape. We have made some preliminary progress in this direction. A second natural question is whether the orbits near the various kind of PRs are chaotic. Our numerical investigation suggests that the orbits structure is very different in each of the cases. Perhaps techniques used in the "dynamic bifurcation" literature may be utilized here [21,29]. A deep open question is the relation of all this to Arnold diffusion or, more precisely, to instability mechanisms in a priori stable systems. We believe that similar mechanisms arising from resonance interactions exist. A precise calculation is yet to be done.

Appendix A. Construction of the phenomenological model

In addition to conditions c1–c3 (Eqs. (2)–(4)), we use the following considerations for the construction of the phenomenological model (7) of a near-integrable 3 d.o.f. Hamiltonian attaining PRs.

By symplectic changes of coordinates, each of the conditions $\langle k, \omega \rangle = 0$; $k \in \mathbb{Z}^2 \setminus \{0\}$ for one resonance, is replaced by the following conditions for vanishing of one of the inner frequencies of the invariant parabolic 2-torus at the origin $O_{xyI_1} := \{(x, y, I_1, I_2) = (0, 0, 0, I_2)\}$. The condition for a 1-resonance, corresponding to the pair $(n, 0), n \in \mathbb{Z} \setminus \{0\}$, is

$$\dot{\theta}_1 = \left. \frac{\partial H_0(x, y, I_1, I_2)}{\partial I_1} \right|_{(0,0,0,0)} = 0. \tag{A.1}$$

Similarly, the condition for a 1-resonance, corresponding to the pair $(0, m)$, $m \in \mathbb{Z} \setminus \{0\}$, is

$$\dot{\theta}_2 = \left. \frac{\partial H_0(x, y, I_1, I_2)}{\partial I_2} \right|_{(0,0,0,\bar{I}_2)} = 0. \tag{A.2}$$

For achieving a 2-resonance, we need the conditions (A.1) and (A.2) to be fulfilled simultaneously on the parabolic torus. Obviously, an external parameter is needed for the 2-resonance condition, let us denote this parameter by α_2

(c4) The condition on the inner frequencies of the parabolic 2-torus for a 2-resonance, corresponding to the pairs $(n, 0)$ and $(0, m)$, for some $n, m \in \mathbb{Z} \setminus \{0\}$, is

$$\nabla_{(I_1, I_2)} H_0(0, 0, 0, I_2 = \alpha_2; \alpha_2 = 0) = (\dot{\theta}_1, \dot{\theta}_2)|_{(0,0,0,0;0)} = (0, 0). \tag{A.3}$$

The phenomenological model (8) (with the Hamiltonian (7)) clearly satisfies the conditions (A.1) and (A.2) for a 1-resonance in I_1 direction (a 2-torus of closed orbits periodic in θ_2) and a 1-resonance in I_2 direction (a 2-torus of closed orbits periodic in θ_1), respectively. Similarly, it satisfies the condition (A.3) for a 2-resonance which corresponds to a normally parabolic 2-torus of fixed points.

To further simplify the model, we add the following assumptions on the near-integrable Hamiltonian H:

(a1) The Hamiltonian is of the form

$$H(x, y, \theta_1, I_1, \theta_2, I_2) = \tfrac{1}{2} y^2 + V(x, I_1, I_2) + O([I_1, I_2]^3, 5),$$

   where V is the potential of the unperturbed system; i.e. the terms in V to order 4 are independent of y and of θ_1, θ_2.

(a2) The action I_1 governs the stability type of the system linearized at the 2D torus corresponding to the equilibrium at the origin of the (x, y) plane, O_{xy}; i.e. it serves like a bifurcation parameter. The action I_2 governs the creation of 1-resonances, and together with the external parameter, α_2, it is responsible for the existence of 2-resonances.

(a3) All the energy surfaces of the Hamiltonian are compact in the (x, y) plane.

(a4) The unstable fixed point, which is created by the pitchfork bifurcation in the (x, y) plane, is shifted to the origin for all I_1, I_2 for which it exists.

Assumption (a1) corresponds to assuming that the Hamiltonian is in the standard form for mechanical Hamiltonian systems which are integrable to quartic order. Assumption (a2) is made for simplicity, and seems to have no effect on the behavior of the system. Moreover, when only the integrable part of the Hamiltonian, H_0, is considered, assumption (a2) is achieved by a symplectic change of variables. Assumption (a3) corresponds to considering the large class of Hamiltonian systems for which the motion in the (x, y) plane must be bounded. Assumption (a4) is made WNLG, and it may be always achieved by a local change of coordinates. Note that under assumptions (a1) and (a2), the parabolicity condition, (c2) (Eq. (3)), may be written in the form

$$\det \left(\left. \frac{\partial^2 V(x, y, I_1, I_2)}{\partial x^2} \right|_{(0,0,0,I_2)} \right) = 0, \quad I_2 \in \mathbb{R}. \tag{A.4}$$

Making a Taylor expansion near the above conditions, rescaling and using the above assumptions result with the Hamiltonian function in Eqs. (7) in Section 2.

Appendix B. Allowed regions of motion

Details of the calculations which lead to identifying the allowed regions of motion in the space of constants of motion of the system (8) are presented for the case $\eta = 0$, $\alpha_1 > -1/2$, and $\alpha_3 \geq 0$. When $\eta = 0$, the integrable

Hamiltonian of the system (8) is

$$H_0(x, y, I; \mu) = \tfrac{1}{2}y^2 - I_1(\tfrac{1}{2}x^2) + \tfrac{1}{4}x^4 + \alpha_2 I_2 + (\tfrac{1}{2} + \alpha_1)\tfrac{1}{2}I_1^2 + \tfrac{1}{2}I_2^2 + \alpha_3 I_1 I_2. \tag{B.1}$$

Since equilibria of the (x, y) system supply boundaries to the energy surfaces of the full system, we find the energy values (Eq. (B.1)) at these points. The fixed points of the integrable system (8) in the (x, y) plane, for $\eta = 0$, are $(0, 0)$ ($I_1 < 0$—elliptic; $I_1 = 0$—parabolic; $I_1 > 0$—hyperbolic) and $(\pm\sqrt{I_1}, 0)$ ($I_1 > 0$—elliptic).

The origin of the (x, y) plane, O_{xy}, is a fixed point for any value of I_1 and I_2. At O_{xy}, (B.1) may be solved for I_1

$$I_{1_{O_{xy}\pm}}(H_0, I_2) = \frac{-2\alpha_3 I_2 \pm 2\sqrt{\alpha_3^2 I_2^2 - (1 + 2\alpha_1)(\alpha_2 I_2 + I_2^2/2 - H_0)}}{1 + 2\alpha_1}. \tag{B.2}$$

For each fixed value of I_2, the curves $I_{1_{O_{xy}-}}(H_0, I_2)$ and $I_{1_{O_{xy}+}}(H_0, I_2)$ form a horizontal parabola in the space (H_0, I_2, I_1). In the energy–momenta bifurcation diagrams, presented in Section 2.1, Figs. 1–5, 6A and 9, these equilibria curves appear as solid curves if they refer to a stable equilibrium, and they appear as dashed curves, if they refer to an unstable equilibrium (and separatrix). The minimal possible value of $H_0(I_2)$, for which the manifolds (B.2) are defined, is found by solving the equation

$$\left.\frac{\partial H_0}{\partial I_1}\right|_{O_{xy}} = 0. \tag{B.3}$$

Notice that $\partial H_0/\partial I_1|_{O_{xy}} = \dot{\theta}_1|_{O_{xy}}$, hence for I_1 values which solve Eq. (B.3), an $(n, 0)$-resonance occurs with respect to the inner frequencies of the corresponding 2-tori. These $I_{1_{\text{res1}}}$ values are

$$I_{1_{\text{res1}}}(I_2) = \frac{-2\alpha_3 I_2}{1 + 2\alpha_1}. \tag{B.4}$$

Substituting (B.4) into Eq. (B.1) at O_{xy} one gets

$$H_{0_{O_{xy}\text{-min}}}(I_2) = \alpha_2 I_2 + \left(\frac{1}{2} - \frac{\alpha_3^2}{1 + 2\alpha_1}\right) I_2^2, \tag{B.5}$$

which is the minimal energy value that should be considered at O_{xy}. Hence, the point $(H_{0_{O_{xy}\text{-min}}}(I_2), I_{1_{\text{res1}}}(I_2))$, obtained from Eqs. (B.4) and (B.5), is the minimal point of the parabolas formed by Eq. (B.2) for each fixed value of I_2.

When $I_1 > 0$, O_{xy} is a hyperbolic fixed point in the (x, y) plane (for any value of I_2). The energy value at the parabolic surface ($I_1 = 0$) is

$$H_{0_p}(I_2) = \alpha_2 I_2 + \tfrac{1}{2}I_2^2. \tag{B.6}$$

Notice that at O_{xyI_1} $((x, y, I_1, I_2) = (0, 0, 0, I_2))$ this energy value corresponds to a normally parabolic 2-torus in the full phase space, for each fixed value of I_2. When I_1 turns to be positive, in addition to the hyperbolic equilibrium at the origin, two elliptic fixed points appear in the (x, y) plane

$$(x_{\text{ell}}, y_{\text{ell}}) = (\pm\sqrt{I_1}, 0). \tag{B.7}$$

Substituting (B.7) into (B.1) one gets

$$H_{0_{\text{ell}}}(I_1, I_2) = \alpha_2 I_2 + \alpha_1(\tfrac{1}{2}I_1^2) + \tfrac{1}{2}I_2^2 + \alpha_3 I_1 I_2. \tag{B.8}$$

Eq. (B.8) may be solved for I_1

$$I_{1_{\text{ell}\pm}}(H_0, I_2) = \frac{-\alpha_3 I_2 \pm \sqrt{I_2^2(\alpha_3^2 - \alpha_1) - 2\alpha_1\alpha_2 I_2 + 2\alpha_1 H_0}}{\alpha_1}. \tag{B.9}$$

For each fixed value of I_2, the curves from Eq. (B.9) may be seen in Figs. 1–5, 6A and 9 as solid curves for positive values of I_1, as they denote elliptic equilibria. For $\alpha_1 > 0$ ($-1/2 < \alpha_1 < 0$) the minimal (maximal) energy value, for which the manifolds in Eq. (B.9) are defined, is

$$H_{0_{\text{ell-min}}}(I_2) = \alpha_2 I_2 + \left(\frac{1}{2} - \frac{\alpha_3^2}{2\alpha_1}\right) I_2^2, \tag{B.10}$$

and it is achieved at

$$I_{1_{\text{ell-res}}}(I_2) = \frac{-\alpha_3 I_2}{\alpha_1}. \tag{B.11}$$

However, the manifolds $I_{1_{\text{ell}\pm}}(H_0, I_2)$ are defined only when the right-hand side of (B.9) is positive. Hence, $H_{0_{\text{ell-min}}}(I_2)$ is their minimal ($\alpha_1 > 0$) or maximal ($-1/2 < \alpha_1 < 0$) energy value only if α_1 and I_2 are of opposite signs. Otherwise, their minimal ($\alpha_1 > 0$) or maximal ($-1/2 < \alpha_1 < 0$) energy value is $H_{0_p}(I_2)$ (Eq. (B.6)). Notice that when α_1 and I_2 are of opposite signs, and $I_1 = I_{1_{\text{ell-res}}}(I_2)$ (from Eq. (B.11)), the elliptic fixed points in the (x, y) plane correspond to normally elliptic resonant 2-tori in the full phase space (for the same reasoning like above for O_{xy}).

When $\alpha_1 = 0$ the manifolds (B.9) cease to exist. For $I_2 \neq 0$ they are replaced by the manifold

$$I_{1_{\text{ell0}}}(H_0, I_2) = \frac{2H_0 - 2\alpha_2 I_2 - I_2^2}{2\alpha_3 I_2}, \tag{B.12}$$

and for $I_2 = 0$ they are replaced by the line $H_0 \equiv 0$. Since for each fixed value of I_2, the curves in (B.9) and (B.12), and the line $H_0 \equiv 0$, refer to a stable equilibrium, they are denoted by solid curves in the bifurcation diagrams, presented in Fig. 3a–c, respectively.

Now let us determine which is the minimal energy value, when such exists, that should be considered for different parameter and variable's values. First of all, let as note that when $\alpha_1 \geq 0$ (or when $\alpha_1 \leq -0.5$), $H_{0_{\text{ell-min}}}(I_2) \leq H_{0_{O_{xy}\text{-min}}}(I_2)$, and when $-0.5 \leq \alpha_1 \leq 0$, $H_{0_{O_{xy}\text{-min}}}(I_2) \leq H_{0_{\text{ell-min}}}(I_2)$. As the next step, we continue to determine the domain of definition of the Hamiltonian equation (B.1). Eq. (B.1) may be rewritten in the form

$$\tfrac{1}{2}y^2 = H_0 + I_1(\tfrac{1}{2}x^2) - \tfrac{1}{4}x^4 - \alpha_2 I_2 - (\tfrac{1}{2} + \alpha_1)\tfrac{1}{2}I_1^2 - \tfrac{1}{2}I_2^2 - \alpha_3 I_1 I_2, \tag{B.13}$$

which imply that the right-hand side of (B.13) must be non-negative. When $x = 0$, the right-hand side of (B.13) is non-negative for

$$I_1 \in [I_{1_{O_{xy}-}}(H_0, I_2), I_{1_{O_{xy}+}}(H_0, I_2)], \tag{B.14}$$

($I_{1_{O_{xy}\pm}}(H_0, I_2)$ are as in (B.2)). Moreover, it follows from (B.13) that for $\alpha_1 \geq 0$ and $I_2 \geq 0$, $H_{0_{O_{xy}\text{-min}}}(I_2)$ (Eq. (B.5)) is the minimal energy value that should be considered: i.e., when $I_{1_{\text{res1}}}(I_2) \leq 0$, $H_{0_{O_{xy}\text{-min}}}(I_2)$ is the minimal energy value for which motion is allowed (see e.g. Fig. 4a). Note that if $I_{1_{\text{res1}}}(I_2) < 0$, the points $(H_0, I_2, I_1) = (H_{0_{O_{xy}\text{-min}}}(I_2), I_2, I_{1_{\text{res1}}}(I_2))$ correspond to elliptic resonant tori, and if $I_{1_{\text{res1}}}(0) = 0$, the point $(H_0, I_2, I_1) = (0, 0, 0)$ corresponds to a parabolic resonant torus (see e.g. Fig. 4b). When $x = \pm\sqrt{I_1}$, $\alpha_1 \geq 0$ and $I_2 < 0$, the right-hand side of (B.13) is non-negative for

$$I_1 \in [I_{1_{\text{ell}-}}(H_0, I_2), I_{1_{\text{ell}+}}(H_0, I_2)] \tag{B.15}$$

for positive I_1 values, there the manifolds (B.9) are defined. Moreover, it follows from Eq. (B.13), that $H_{0_{\text{ell-min}}}(I_2)$ is the minimal energy value that should be considered for $\alpha_1 > 0$ and $I_2 < 0$ (see Fig. 4c).

Continuing with similar considerations we conclude: For $\alpha_1 > 0$, the minimal energy value for which motion is allowed is $H_{0_{O_{xy}\text{-min}}}(I_2)$ when $I_2 \geq 0$, and $H_{0_{\text{ell-min}}}(I_2)$ when $I_2 < 0$. For $\alpha_1 = 0$, the minimal energy value is

$H_{0_{O_{xy}\text{-min}}}(I_2)$ when $I_2 \geq 0$. For $\alpha_1 = 0$ and $I_2 < 0$, and for $-1/2 < \alpha_1 < 0$ and any value of I_2, minimal energy value does not exist, and motion is allowed for *all* energy values (see e.g. Fig. 2).

For the considered parameter values, the energy surfaces are always bounded from below in I_1 direction. The bounding manifold from below in I_1 direction may be either one of the manifolds: $I_{1_{O_{xy}-}}(H_0, I_2)$, $I_{1_{ell-}}(H_0, I_2)$, $I_{1_{ell0}}(H_0, I_2)$, depending on the range of energy, I_2 and α_1 values (for each fixed triple (H_0, I_2, α_1) only one of these is defined). For $\alpha_1 > 0$ the energy surfaces are bounded from above in I_1 direction: When $I_2 \geq 0$, the upper bound is either the *stable part* of $I_{1_{O_{xy}+}}(H_0, I_2)$ or of $I_{1_{ell+}}(H_0, I_2)$, depending on the range of the energy values (again, for each energy value, only one of these exists). When $I_2 < 0$, the upper bound is $I_{1_{ell+}}(H_0, I_2)$ for all allowed energy values. For $\alpha_1 = 0$, the energy surfaces are bounded from above in I_1 direction only for positive I_2 values, by the manifold $I_{1_{ell0}}(H_0, I_2)$. For all other values of α_1 and of I_2, the energy surfaces are unbounded from above in I_1 direction. The regions of allowed motion between or above the equilibria bounds are denoted by vertical lines in Figs. 2–6.

See Table 1 for a summary and full description of the regions in (H_0, I_2, I_1) space where motion is allowed for different values of the parameter α_1.

Remark 7. In all the tables, for simplicity of notation, we use $H_{0_{O_{xy}\text{-min}}} := H_{0_{O_{xy}\text{-min}}}(I_2)$, $H_{0_p} := H_{0_p}(I_2)$, $H_{0_{ell\text{-min}}} := H_{0_{ell\text{-min}}}(I_2)$, $I_{1_{O_{xy}\pm}} := I_{1_{O_{xy}\pm}}(H_0, I_2)$, $I_{1_{ell\pm,0}} := I_{1_{ell\pm,0}}(H_0, I_2)$, $I_{1_{\Delta\pm,0}} := I_{1_{\Delta\pm,0}}(H_0, I_2)$, $I_{1_{res1}} := I_{1_{res1}}(I_2)$.

Table 1
The domain of definition of the integrable Hamiltonian equation (B.1)-allowed regions of motion in the space of constants of motion (H_0, I_2, I_1)

	$\alpha_1 > 0$	$\alpha_1 = 0$	$-\frac{1}{2} < \alpha_1 < 0$
$I_2 > 0$	$H_0 \in [H_{0_{O_{xy}-\text{min}}}, H_{0_p}]$ $\Rightarrow I_1 \in [I_{1_{O_{xy}-}}, I_{1_{O_{xy}+}}]$, $H_0 \geq H_{0_p}$ $\Rightarrow I_1 \in [I_{1_{O_{xy}-}}, I_{1_{ell+}}]$	$H_0 \in [H_{0_{O_{xy}-\text{min}}}, H_{0_p}]$ $\Rightarrow I_1 \in [I_{1_{O_{xy}-}}, I_{1_{O_{xy}+}}]$, $H_0 \geq H_{0_p}$ $\Rightarrow I_1 \in [I_{1_{O_{xy}-}}, I_{1_{ell0}}]$	$H_0 \leq H_{0_{O_{xy}-\text{min}}}$ $\Rightarrow I_1 \in [I_{1_{ell-}}, \infty)$, $H_0 \in [H_{0_{O_{xy}-\text{min}}}, H_{0_p}]$ $\Rightarrow I_1 \in [I_{1_{O_{xy}-}}, I_{1_{O_{xy}+}}]$ $\cup [I_{1_{ell-}}, \infty)$, $H_0 \geq H_{0_p}$ $\Rightarrow I_1 \in [I_{1_{O_{xy}-}}, \infty)$
$I_2 = 0$	$H_0 \geq 0$ $\Rightarrow I_1 \in [I_{1_{O_{xy}-}}, I_{1_{ell+}}]$	$H_0 \geq 0$ $\Rightarrow I_1 \in [I_{1_{O_{xy}-}}, \infty)$	$H_0 \leq 0$ $\Rightarrow I_1 \in [I_{1_{ell-}}, \infty)$, $H_0 \geq 0$ $\Rightarrow I_1 \in [I_{1_{O_{xy}-}}, \infty)$
$I_2 < 0$	$H_0 \in [H_{0_{ell-\text{min}}}, H_{0_p}]$ $\Rightarrow I_1 \in [I_{1_{ell-}}, I_{1_{ell+}}]$, $H_0 \geq H_{0_p}$ $\Rightarrow I_1 \in [I_{1_{O_{xy}-}}, I_{1_{ell+}}]$	$H_0 \leq H_{0_{O_{xy}-\text{min}}}$ $\Rightarrow I_1 \in [I_{1_{ell0}}, \infty)$, $H_0 \in [H_{0_{O_{xy}-\text{min}}}, H_{0_p}]$ $\Rightarrow I_1 \in [I_{1_{O_{xy}-}}, I_{1_{O_{xy}+}}]$ $\cup [I_{1_{ell0}}, \infty)$, $H_0 \geq H_{0_p}$ $\Rightarrow I_1 \in [I_{1_{O_{xy}-}}, \infty)$	$H_0 \leq H_{0_p}$ $\Rightarrow I_1 \in [I_{1_{ell-}}, \infty)$, $H_0 \geq H_{0_p}$ $\Rightarrow I_1 \in [I_{1_{O_{xy}-}}, \infty)$

The regions of allowed motion are calculated for constructing the energy–momenta bifurcations diagrams by fixing a value of I_2, and then obtaining the range of the allowed values of H_0 and I_1 for which the Hamiltonian equation is well defined. On the other hand, if specific energy surface is to be analyzed, one may want to fix the energy value and to obtain the allowed values of I_1 and I_2 for which the Hamiltonian is defined on this particular energy surface (e.g. see Fig. 6B).

The curves defining the region(s) of I_2 values, for a fixed energy value, H_0, and such that the I_1 values are defined by the curves: $I_{1_{O_{xy}\pm}}(H_0, I_2)$ and $I_{1_{\text{ell}\pm}}(H_0, I_2)$ (Eqs. (B.2) and (B.9)), calculated above, are

$$I_{2_{O_{xy}\pm}} = \frac{-(1 + 2\alpha_1)\alpha_2 \pm \sqrt{\alpha_2^2(1 + 2\alpha_1)^2 + 4(-\alpha_3^2 + 0.5 + \alpha_1)(1 + 2\alpha_1)H_0}}{1 + 2\alpha_1 - 2\alpha_3^2}, \tag{B.16}$$

which define for $\alpha_1 - \alpha_3^2 \neq -1/2$ a parabola attaining its maxima (for $\alpha_1 - \alpha_3^2 < -1/2$) or minima (for $\alpha_1 - \alpha_3^2 > -1/2$) at the critical value of H_0

$$H_{0_{gm\pm}} = -\frac{\alpha_2^2(1 + 2\alpha_1)}{2(1 + 2(\alpha_1 - \alpha_3^2))}, \tag{B.17}$$

and

$$I_{2_{\text{ell}\pm}} = \frac{-\alpha_1\alpha_2 \pm \sqrt{(\alpha_1\alpha_2)^2 + 2(-\alpha_3^2 + \alpha_1)\alpha_1 H_0}}{\alpha_1 - \alpha_3^2}, \tag{B.18}$$

which define, for $\alpha_1 - \alpha_3^2 \neq 0$, a parabola attaining its maxima (for $\alpha_1 - \alpha_3^2 < 0$) or minima (for $\alpha_1 - \alpha_3^2 > 0$) at the critical value of H_0

$$H_{0_{gm-\text{ell}}} = -\frac{\alpha_1\alpha_2^2}{2(\alpha_1 - \alpha_3^2)}. \tag{B.19}$$

For the parameter values for which these parabolas attaining minima, the values of I_2 for which the corresponding parabolas defining the values of I_1 (Eqs. (B.2) and (B.9)), for a given energy value, H_0, are defined inside the parabola. Hence the corresponding energy surface is continuous and bounded in I_2 if $H_0 \geq H_{0_{gm-\text{ell}}}$, and there are no values of I_2 for which motion is allowed if $H_0 < H_{0_{gm-\text{ell}}}$ (i.e. no energy surface exists for this value of H_0). When both parabolas attaining a maxima, the energy surface is unbounded in I_2 (as then the allowed I_2 values are outside the parabolas), where for energy values $H_0 \geq H_{0_{gm\pm}}$ the energy surface is defined for all I_2 values, and for $H_0 < H_{0_{gm\pm}}$ the corresponding energy surface may be connected, or disconnected, in I_2. When $-1/2 < \alpha_1 - \alpha_3^2 < 0$, (B.16) attaining a minima and (B.18) attaining a maxima, the energy surfaces behave in a similar way. At the degenerate points ($\alpha_1 = \alpha_3^2$ and $\alpha_1 = \alpha_3^2 - 1/2$), for which these parabolas cease to exist, lines which define the allowed I_2 values, replace the parabolas (B.16) and (B.18). At the degenerate points flat PRs appear for certain values of I_2.

Appendix C. Regions of back-flow

Here we seek I_1 values for which back-flow occurs in the allowed regions of motion, i.e. we seek values of I_1 for which the right-hand side of Eq. (B.13) is non-negative, and $\dot{\theta}_1 = 0$. At O_{xy}, $\dot{\theta}_1 = 0$ for $I_{1_{\text{res1}}}(I_2)$ (Eq. (B.4)). Assuming that $\dot{\theta}_1 = 0$ for some x value, x^2 may be eliminated from the third equation of the integrable system (8)

$$x_{\text{res}}^2(I_1, I_2) = (1 + 2\alpha_1)I_1 + 2\alpha_3 I_2. \tag{C.1}$$

Table 2
The regions where $\dot{\theta}_1$ changes sign and backflow occurs

	$\alpha_1 > 0$	$\alpha_1 = 0$	$-\frac{1}{2} < \alpha_1 < 0$
$I_2 > 0$	$I_1 \in [I_{1_{res1}}, I_{1_{\Delta+}}]$	$I_1 \in [I_{1_{res1}}, I_{1_{\Delta 0}}]$	$H_0 \le H_{0_{end}} \Rightarrow$ $I_1 \in [I_{1_{res1}}, I_{1_{\Delta+}}]$ $\cup \ [I_{1_{\Delta-}}, \infty)$, $H_0 \ge H_{0_{end}} \Rightarrow$ $I_1 \in [I_{1_{res1}}, \infty)$
$I_2 = 0$	$I_1 \in [I_{1_{res1}}, I_{1_{\Delta+}}]$	$I_1 \in [I_{1_{res1}}, \infty)$	$H_0 \le H_{0_{min}} \Rightarrow$ $I_1 \in [I_{1_{\Delta-}}, \infty)$, $H_0 \ge H_{0_{min}} \Rightarrow$ $I_1 \in [I_{1_{res1}}, \infty)$
$I_2 < 0$	$H_0 \in [H_{0_{end}}, H_{0_{min}}]$ $\Rightarrow I_1 \in [I_{1_{\Delta-}}, I_{1_{\Delta+}}]$, $H_0 \ge H_{0_{min}}$ $\Rightarrow I_1 \in [I_{1_{res1}}, I_{1_{\Delta+}}]$	$H_0 \le H_{0_{min}} \Rightarrow$ $I_1 \in [I_{1_{\Delta 0}}, \infty)$, $H_0 \ge H_{0_{min}} \Rightarrow$ $I_1 \in [I_{1_{res1}}, \infty)$	$H_0 \le H_{0_{min}} \Rightarrow$ $I_1 \in [I_{1_{\Delta-}}, \infty)$, $H_0 \ge H_{0_{min}} \Rightarrow$ $I_1 \in [I_{1_{res1}}, \infty)$

Hence, $\dot{\theta}_1$ may vanish only when the right-hand side of Eq. (C.1) is non-negative. Therefore, it follows that $\dot{\theta}_1$ may change sign along orbits only if $I_1 \ge I_{1_{res1}}(I_2)$. Substituting (C.1) into the right-hand side of (B.13) and solving for I_1 one gets

$$I_{1_{\Delta\pm}}(H_0, I_2) = \frac{-\alpha_3 I_2}{\alpha_1} \pm \frac{\sqrt{\alpha_3^2 I_2^2 + \alpha_1(2H_0 - I_2(2\alpha_2 + I_2))}}{\alpha_1 \sqrt{1 + 2\alpha_1}}, \tag{C.2}$$

where $I_1 \in [I_{1_{\Delta-}}(H_0, I_2), I_{1_{\Delta+}}(H_0, I_2)]$ if $\alpha_1 > 0$ and $I_1 \in]I_{1_{\Delta+}}(H_0, I_2), I_{1_{\Delta-}}(H_0, I_2)[$ if $-1/2 < \alpha_1 < 0$. The manifolds in (C.2) are defined for $H_0 \ge H_{0_{\text{ell-min}}}$ when $\alpha_1 > 0$, and for $H_0 \le H_{0_{\text{ell-min}}}$ when $-1/2 < \alpha_1 < 0$. They cease to exist when $\alpha_1 = 0$, where they are replaced by the manifold

$$I_{1_{\Delta 0}}(H_0, I_2) = \frac{H_0 - \alpha_2 I_2 - I_2^2(1/2 + \alpha_3^2)}{\alpha_3 I_2}, \tag{C.3}$$

where $I_1 \le I_{1_{\Delta 0}}(H_0, I_2)$ for $I_2 > 0$ and $I_1 \ge I_{1_{\Delta 0}}(H_0, I_2)$ for $I_2 < 0$. For $\alpha_1 = I_2 = 0$ none of these manifolds (C.2) and (C.3) is defined.

Hence, back-flow occurs for I_1 values which are in the specified above ranges, and are greater or equal to $I_1 = I_{1_{res1}}(I_2)$. The summary of where $\dot{\theta}_1$ changes its sign on a given energy surface is given in Table 2 (the shaded area in Figs. 1–6 and 9). The special back-flow orbit structure in the (θ_1, x) plane may be seen, e.g., in Fig. 8c.

Note that when $\dot{\theta}_1$ vanishes on an equilibrium point of the (x, y) plane, a resonance occurs. It happens for $I_1 = I_{1_{res1}}(I_2)$ (Eq. (B.4)) at O_{xy}, and if α_1 and I_2 are of opposite signs, for $I_1 = I_{1_{\text{ell-res}}}(I_2)$ (Eq. (B.11)) at $(x, y) = (\pm\sqrt{I_1}, 0)$. We denote these resonance values of I_1 by asterisks in the bifurcation diagrams presented in Figs. 1–5, 6A and 9.

On a given energy surface, $\dot{\theta}_1$ vanishes on the separatrix if:

- $I_2 > 0$, $H_0 \ge H_{0_p}(I_2)$ and:
  $\alpha_1 > 0$, $I_{1_{\Delta+}}(H_0, I_2) \ge I_{1_{O_{xy}+}}(H_0, I_2)$ or

$-1/2 < \alpha_1 < 0, I_{1_{\Delta-}}(H_0, I_2) \geq I_{1_{O_{xy+}}}(H_0, I_2)$ or

$\alpha_1 = 0, I_{1_{\Delta 0}}(H_0, I_2) \geq I_{1_{O_{xy+}}}(H_0, I_2)$.

- $I_2 < 0$ and:

  $\alpha_1 > 0, I_{1_{\Delta+}}(H_0, I_2) \geq I_{1_{O_{xy+}}}(H_0, I_2)$ or

  $-1/2 < \alpha_1 < 0, I_{1_{\Delta-}}(H_0, I_2) \geq I_{1_{O_{xy+}}}(H_0, I_2)$ or

  $\alpha_1 = 0, I_{1_{\Delta 0}}(H_0, I_2) \geq I_{1_{O_{xy+}}}(H_0, I_2)$.

- $I_2 = 0$ and:

  $\alpha_1 > 0, I_{1_{\Delta+}}(H_0, I_2) \geq I_{1_{O_{xy+}}}(H_0, I_2)$ or

  $-1/2 < \alpha_1 < 0, I_{1_{\Delta-}}(H_0, I_2) \geq I_{1_{O_{xy+}}}(H_0, I_2)$ or

  $\alpha_1 = 0$.

References

[1] V.I. Arnol'd, Proof of a theorem of A. N. Kolmogorov on the invariance of quasi-periodic motions under small perturbations of the Hamiltonian, Russ. Math. Surv. 18 (5) (1963) 9–36.

[2] V.I. Arnol'd, Instability of dynamical systems with several degrees of freedom, Dokl. Akad. Nauk SSSR (Russian) 156 (1) (1964) 9–12 [English translation in Sov. Math. Dokl. 5, 581–585].;
V.I. Arnol'd, Russian Math. Surv. 18 (1964) 85.

[3] V.I. Arnol'd, Mathematical Methods of Classical Mechanics, Springer, Berlin, 1978.

[4] V.I. Arnol'd, Dynamical Systems III, 2nd Edition, Vol. 3 of Encyclopedia of Mathematical Sciences, Springer, Berlin, 1993.

[5] S. Bolotin, R.S. MacKay, Multibump orbits near the anti-integrable limit for Lagrangian systems, Nonlinearity 10 (1997) 1015–1029.

[6] S. Bolotin, D. Treschev, Unbounded growth of energy in nonautonomous Hamiltonian systems, Nonlinearity 12 (2) (1999) 365–388.

[7] A.V. Bolsinov, A.T. Fomenko, Trajectory classification of simple integrable Hamiltonian systems on three-dimensional surfaces of constant energy, Dokl. Akad. Nauk (Russian) 332 (5) (1993) 553–555 [English translation in Russian Acad. Sci. Dokl. Math. 48 (2) (1994) 365–369].

[8] B.L.J. Braaksma, H.W. Broer, G.B. Huitema, Towards a quasi-periodic bifurcation theory, Mem. AMS 83 (421) (1990) 82–175.

[9] H.W. Broer, G.B. Huitema, M.B. Sevryuk, Quasi-periodic Tori in Families of Dynamical Systems: Order Amidst Chaos, LNM 1645, Springer, Berlin, 1996.

[10] A. Delshams, R. de la Llave, T.M. Seara, A geometric approach to the existence of orbits with unbounded energy in generic periodic perturbations by a potential of generic geodesic flows of $\mathbb{T}^2$, Commun. Math. Phys. 209 (2) (2000) 353–392.

[11] H.R. Dullin, M. Juhnke, P.H. Richter, Action integrals and energy surfaces of the kovalevskaya top, Int. J. Bifur. Chaos Appl. Sci. Eng. 4 (6) (1994) 1535–1562.

[12] R.W. Easton, J.D. Meiss, G. Roberts, Drift by coupling to an anti-integrable limit, Preprint, August 2000.

[13] L.H. Eliasson, Perturbations of stable invariant tori for hamiltonian systems, Ann. Scuola Norm. Sup. Pisa Cl. Sci. IV 15 (1) (1988) 115–147.

[14] N. Fenichel, Persistence and smoothness of invariant manifolds for flows, Ind. Univ. Math. J. 21 (1971) 193–225.

[15] A.T. Fomenko, Topological classification of all integrable hamiltonian differential equations of general type with two degrees of freedom, in: The Geometry of Hamiltonian Systems, Vol. 22, Mathematical Science Research Institute Publication, Berkeley, CA, Springer, New York, 1989, 1991, pp. 131–339.

[16] S.M. Graff, On the conservation of hyperbolic invariant tori for Hamiltonian systems, J. Diff. Eq. 15 (1974) 1–69.

[17] G. Haller, Chaos Near Resonance, Applied Mathematical Sciences, Vol. 138, Springer, New York, 1999.

[18] G. Haller, S. Wiggins, Multi-pulse jumping orbits and homoclinic trees in a modal truncation of the damped-forced nonlinear schrödinger equation, Physica D 85 (3) (1995) 311–347.

[19] G. Haller, S. Wiggins, Geometry and chaos near resonant equilibria of 3 d.o.f. Hamiltonian systems, Physica D 90 (4) (1996) 319–365.

[20] H. Hanßmann, The quasi-periodic center-saddle bifurcation, J. Diff. Eq. 142 (2) (1997) 305–370.

[21] N. Lebovitz, A. Pesci, Dynamic bifurcations in Hamiltonian systems with one degree of freedom, SIAM J. Appl. Math. 55 (4) (1995) 1117–1133.

[22] L.M. Lerman, I.L. Umanskii, Classification of four-dimensional integrable Hamiltonian systems and poisson actions of $\mathbb{R}^2$ in extended neighborhoods of simple singular points I, Math. Sb. (Russian) 183 (12) (1992); English translation in Russian Acad. Sci. Sb. Math. 77 (2) (1994) 511–542.

[23] L.M. Lerman, I.L. Umanskii, Classification of four-dimensional integrable Hamiltonian systems and poisson actions of $\mathbb{R}^2$ in extended neighborhoods of simple singular points II, Math. Sb. (Russian) 184 (4) (1993) 105–138 [English translation in Russian Acad. Sci. Sb. Math. 78 (2) (1994) 479–506].

[24] L.M. Lerman, I.L. Umanskii, Classification of four-dimensional integrable Hamiltonian systems and poisson actions of $\mathbb{R}^2$ in extended neighborhoods of simple singular points. III. Realizations, Math. Sb. (Russian) 186 (10) (1995) 89–102 [English translation in Sb. Math. 186 (10) (1995) 1477–1491].

[25] A.J. Lichtenberg, M.A. Lieberman, Regular and Stochastic Motion, Vol. 38, Applied Mathematical Sciences, Springer, Berlin, 1983.
[26] A. Litvak-Hinenzon, Parabolic resonances in near-integrable Hamiltonian systems, Ph.D. Thesis, The Weizmann Institute of Science, Rehovot, Israel, May 2001 (Advisor: V. Rom-Kedar).
[27] A. Litvak-Hinenzon, V. Rom-Kedar, Resonant tori and instabilities in Hamiltonian systems, submitted for publication, preprint: http://www.ma.utexas.edu/mp\arc-bin/mpa?yn=01-177.
[28] A. Litvak-Hinenzon, V. Rom-Kedar, Parabolic resonances in near-integrable Hamiltonian systems, in: D.S. Broomhead, E.A. Luchinskaya, P.V.E. McClintock, T. Mullin (Eds.), Stochaos: Stochastic and Chaotic Dynamics in the Lakes, American Institute of Physics, Melville, New York, USA, 2000, pp. 358–368 (refereed).
[29] G. Mareé, Slow passage through a pitchfork bifurcation, SIAM J. Appl. Math. 56 (3) (1996) 889–918.
[30] J.N. Mather, Graduate Course in Princeton, 1995–1996, and Lectures at Penn State, Spring 1996, Paris, Summer 1996, Austin, Fall 1996.
[31] A.A. Oshemkov, Description of isoenergetic surfaces of integrable Hamiltonian systems with two degrees of freedom, Trudy Sem. Vektor. Tenzor. Anal. 23 (1988) 122–132 (in Russian).
[32] N. Paldor, E. Boss, Chaotic trajectories of tidally perturbed inertial oscillations, J. Atmos. Sci. 49 (1992) 2306–2318.
[33] J. Pöschel, On elliptic lower dimensional tori in Hamiltonian systems, Math. Z. 202 (1989) 559–608.
[34] V. Rom-Kedar, Parabolic resonances and instabilities, Chaos 7 (1) (1997) 148–158.
[35] V. Rom-Kedar, Y. Dvorkin, N. Paldor, Chaotic Hamiltonian dynamics of particle's horizontal motion in the atmosphere, Physica D 106 (1997) 389–431.
[36] V. Rom-Kedar, N. Paldor, From the tropics to the poles in forty days, Bull. Am. Meteorol. Soc. 78 (12) (1997) 2779–2784.
[37] D.V. Treschev, Multidimensional simplectic separatrix maps, Preprint.
[38] Z. Xia, Arnold diffusion: a variational construction, in: Proceedings of the International Congress of Mathematicians, Vol. II, Doc. Math., Extra Vol. ICM II, Berlin, 1998, pp. 867–877.
[39] G. Zaslavsky, R. Sagdeev, D. Usikov, A. Chernikov, Minimal chaos, stochastic webs and structures of quasicrystal symmetry, Sov. Phys. Usp. 31(10) (1988) and references therein.